

PFC/JA-85-43

Poloidal Asymmetries in the Scrape-Off
Layer Plasma of the Alcator C Tokamak

LaBombard, B., Lipschultz, B.

May 1986

Plasma Fusion Center
Massachusetts Institute of Technology
Cambridge, MA 02139

Submitted for publication in: Nuclear Fusion

By acceptance of this article, the publisher and/or recipient acknowledges the U.S. Government's right to retain a non-exclusive, royalty-free license in and to any copyright covering this paper.

POLOIDAL ASYMMETRIES IN THE SCRAPE-OFF LAYER PLASMA OF THE ALCATOR C TOKAMAK

B. LABOMBARD, B. LIPSCHULTZ

*Plasma Fusion Center
Massachusetts Institute of Technology
Cambridge, Massachusetts, U.S.A.*

Abstract: Large poloidal asymmetries in density, electron temperature, radial density e-folding length, and floating potential have been measured in the plasma which exists between the limiter radius and the wall of the Alcator C tokamak. Factors of ~ 4 -20 variation in density and ~ 3 -8 variation in radial density e-folding length are typically recorded in discharges which are bounded by poloidally symmetric ring limiters. These poloidal asymmetries show that pressure is not constant on a magnetic flux surface in this plasma region. Observations of toroidally symmetric MARFE phenomena further imply that pressure is not constant on closed flux surfaces existing just inside the limiter radius. The magnitude of the poloidal asymmetry and its functional dependence on poloidal angle persists independent of machine parameters (central plasma density, plasma current, toroidal field, MARFE versus non-MARFE discharges). Analysis of the data indicates that these asymmetries are caused by perpendicular particle and heat transport asymmetries in both the main plasma and the scrape-off layer. A number of asymmetric perpendicular transport processes are examined in the scrape-off layer plasma including diffusion and $\underline{E} \times \underline{B}$ plasma convection.

Table of Contents

Abstract	i
Contents	1
1. Introduction.	2
2. Experiment Description	4
3. DENSEPACK Measurements.	5
3.1 Density.	5
3.2 Temperature	7
3.3 Pressure	8
3.4 Density Scrape-off Length (λ_n)	9
3.5 Floating Potential	10
3.6 Fluctuations	11
A. Power Spectrum	12
B. Correlations	12
C. Spatial Variation of Fluctuation Amplitude	14
4. Mechanisms Supporting Poloidal Asymmetry	15
4.1 Check of Systematic Errors.	15
A. DENSEPACK Installation.	15
B. DENSEPACK Perturbations.	16
4.2 Magnetic Flux Surfaces	17
A. Poloidal Contours of Constant $\log(P_e)$	17
B. Constant Flux Contour Plots.	18
4.3 Spatially Dependent Diffusion.	18
A. Scrape-off Length Variation: Spatially Dependent Diffusion	19
B. Scrape-off Length Variation: Directed \tilde{n} , $\tilde{\Phi}$ Fluxes	21
4.4 Perpendicular Convection	23
A. Perpendicular Convection Transport Terms	23
B. Magnitude of Perpendicular Convection Terms from $\nabla\Phi_s$ Data	25
C. Scrape-off Length Variation: Spatially Dependent Convection	26
5. Poloidal Asymmetries Inside the Limiter Radius	28
6. Summary	30
Acknowledgements	31
References	32
Figures	34

1. Introduction

The plasma existing in the shadow of the limiter (SOL plasma) plays an important role in the operation of tokamaks. Impurities found in the main plasma are derived from interaction of the SOL plasma with the limiter and other vacuum vessel components. There is also experimental evidence that plasma near the plasma boundary (minor radius, $r \approx$ limiter radius, a) can strongly affect the global energy confinement time (H-mode) [1-3]. Furthermore, plasma parameters of the SOL are a reflection of heat and particle fluxes originating from $r \lesssim a$, an area which is generally difficult to diagnose by direct means.

Recognizing the importance of the edge plasma, there has been an increased emphasis on diagnosing the SOL plasma of tokamaks, particularly through the use of probes. Typical edge plasma densities ($n \sim 10^{11}-10^{14}/\text{cm}^3$) and temperatures ($T_e \sim 5-50$ eV) are within the operating range of probe systems which can employ one or a number of diagnostics such as Langmuir probes, heat flux probes, and retarding field energy analyzers. Such diagnostic systems on many tokamaks have been very useful in parameterizing the edge plasma state. It is typically observed that perpendicular transport in the edge plasma is highly anomalous with estimates for the perpendicular diffusion coefficient exceeding the level of Bohm diffusion [4]. This anomalous level of particle and energy transport is often attributed to density and potential fluctuations [5]. Probe systems designed to specifically study fluctuations have yielded much information on turbulent transport in the SOL plasma and indicate that electrostatic fluctuations are indeed important in driving particle and energy transport in this region [6,7].

One limitation in most of these studies is the inability to cover a large poloidal or toroidal extent of the SOL plasma. Often a SOL probe system will reside at one poloidal and toroidal position and scan in minor radius. In principle, a composite picture of the edge plasma can be constructed with such a system by moving the probe to various poloidal and toroidal locations and repeating the radial scan. However, this method is subject to the variability of discharge conditions and involves a large amount of dedicated run time. More typically, an assumption is made about the toroidal and/or poloidal symmetry of the SOL plasma, and the corresponding data analysis proceeds on this basis.

Recent observations of tokamak plasmas suggest that this assumption of symmetry is often violated. This is most evident in the detection of poloidally asymmetric MARFE phenomena on a number of tokamaks [8-12]. The Alcator C tokamak employs a poloidally symmetric ring limiter system to scrape-off the edge plasma. Yet, in addition to MARFEs, poloidal asymmetries are detected in this tokamak through the observation of asymmetric damage patterns on vacuum vessel components (limiters and vacuum vessel weld guard rings) [13]. One implication of these observations is that the edge plasma is not only poloidally asymmetric, but may also violate the usual assumption of constant pressure on a closed magnetic flux surface.

Single spatial point probe measurements which are most typically made in the SOL plasma cannot readily examine this question of pressure symmetry on a magnetic flux surface in the edge plasma of tokamaks. However, in tokamaks with circular magnetic flux surfaces and circular poloidal limiters, such as in Alcator C, asymmetries on a flux surface can be directly investigated with a multiple probe system that simultaneously samples plasma at fixed minor radii and various poloidal angles.

Motivated by the above observations of poloidally asymmetric phenomena in Alcator C and other tokamaks, we have utilized an array of 80 closely spaced Langmuir probes to study variations in edge parameters over nearly the full 360° poloidal extent of the SOL plasma of Alcator C at a fixed toroidal position. As originally suspected, the SOL plasma was found to display strong poloidal asymmetries in plasma density and temperature. However, these asymmetries were found to be unexpectedly large and to persist independent of machine parameters (central plasma density, plasma current, toroidal field, MARFE versus non-MARFE discharges). Furthermore, these asymmetries directly indicated that pressure was not constant on a flux surface in the SOL plasma of Alcator C. These large poloidal asymmetries detected by this densely packed Langmuir probe diagnostic (DENSEPACK) and mechanisms which might support such asymmetries are the primary focus of this paper.

Following a brief description of the experimental equipment in section 2, section 3 presents typical poloidal variations in Alcator C edge plasma param-

eters as inferred from DENSEPACK data. It is shown that edge density, electron temperature, density scrape-off length, and floating potential are strong functions of poloidal angle. The poloidal location where the MARFE region is typically observed is identified with the position of lowest electron temperature in poloidal angle. However, the poloidally asymmetric structure evident in the SOL is present in both MARFE and non-MARFE discharges. Section 4 discusses mechanisms which may support the observed asymmetries in the SOL plasma. Spatially dependent perpendicular diffusion and convection are considered. In section 5, poloidally asymmetric density profiles inferred at the limiter radius are discussed. The implication is that asymmetric perpendicular transport is also active inside the limiter radius. Finally, section 6 summarizes the major findings of this study.

2. Experiment Description

Alcator C has major and minor radii of 64.0 and 16.5 cm respectively. The range in central plasma parameters accessed during these experiments were toroidal fields of 6–10 tesla, plasma currents of 200–500 kA and central line-averaged densities ranging $1\text{--}5 \times 10^{14}/\text{cm}^3$. The limiter material consisted of graphite blocks covered with a thin (~ 100 micron) coating of SiC, deposited using a chemical-vapor process. The limiter geometry and locations in Alcator C with respect to the DENSEPACK probe array are illustrated in Figure 1. The DENSEPACK probe array resided in *C* port. Sets of two poloidal limiters were located in *B*, *E*, and *F* ports. The limiter sets in *B* and *E* ports consisted of one full and one partial poloidal ring. The limiter set in *F* port consisted of two partial poloidal rings. Each partial ring limiter had a 90° poloidal segment removed on the outside midplane. However, magnetic field lines that passed through this 90° gap at *B* and *E* ports were intercepted by the accompanying full ring limiters. Thus, the edge plasma was scraped off with poloidal uniformity on the DENSEPACK half of the torus.

A schematic of the DENSEPACK probe array is shown in Figure 2. Details of the probe design and electronics system are described in reference [14]. The array consisted of three different length molybdenum probes mounted with ~ 1

cm poloidal spacing on a rigid stainless steel support ring. The different length probes sampled plasma at minor radii of 16.8, 17.2, and 17.6 cm over a poloidal angular extent of 360° excluding two $\sim 40^\circ$ segments at top and bottom. The stainless steel support ring was divided into six segments which were inserted through the access keyhole slots and clamped into place with wedge-shaped expansion blocks. The outer radius of the support ring was designed to press against the vacuum vessel wall, insuring that the ring structure was positioned accurately with respect to minor radius. The inner radius of the support ring was at $r = 18.0$ cm which coincided with the innermost radial extent of nearby vacuum vessel weld guard rings.

Data acquisition electronics allowed 30 probes to be operated simultaneously. A full voltage sweep of each probe tip was accomplished every 5 msec during the experiment. Standard single Langmuir probe analysis then determined the local values of n , T_e and floating potential as a function of poloidal angle, radius, and time. The goal was to map out any poloidal variations in plasma density and temperature over a range of main plasma parameters. Through the use of fast data loggers (1 MHz sampling rate), this system was also used to record fluctuation spectra and to search for large spatial scale fluctuation correlations occurring between probes.

3. DENSEPACK Measurements

3.1 Density

The plasma density in the limiter shadow region of Alcator C was found by DENSEPACK to be a strong function of poloidal angle. Figure 3a displays a 3-D surface representing density at a radius of 16.8 cm versus poloidal angle and time. A single poloidal profile at 250 msec during the flat-top portion of the plasma current is also plotted (Figure 3b). Poloidal angle refers to the coordinate system indicated in Figure 2. The central parameters for this data were line-averaged density, $\bar{n}_e \approx 2 \times 10^{14}/\text{cm}^3$, plasma current, $I_p \approx 350$ kA, and toroidal field, $B_t \approx 8$ tesla, in a deuterium plasma. Each data point was generated from

a fit of two 5 msec Langmuir sweeps folded together. No poloidal or temporal smoothing was performed for the plots in this figure.

The most striking feature in this data is the poloidal variation of the density. Density maxima appear at the top and bottom of the poloidal cross-section while minima appear at the inside and outside. The poloidal variation always followed a $-\cos(2\theta)$ dependence, i.e. with two maxima and minima. The lowest densities for a given radius always appeared on the inside midplane. In fact, some probes along the inside wall were not used on this day because the collection current was found to be too low there.

The sharpest poloidal gradient was detected by two probes near the 270° location. Density changed by $\sim 2 \times 10^{13}/\text{cm}^3$ in a poloidal distance of ~ 3 cm. This poloidal structure was established quickly in the discharge ($\lesssim 20$ msec) and persisted throughout the duration of the discharge. Data in Figure 3 is cutoff in time for display purposes at 400 msec. The structure in the density profile at longer times during current ramp-down remains similar, displaying a smooth, decreasing level to plasma termination.

The top and bottom density peaks shown in Figure 3 achieve roughly the same level, $n_e \approx 5 \times 10^{13}/\text{cm}^3$. However, the usual value for the bottom peak was typically 20% lower than the top peak. When the toroidal field was reversed, the bottom peak became the larger one in an almost symmetric way. This finding is reminiscent of up-down asymmetries in the edge impurity radiation on Alcator A [15] and PDX [16] as well as the pressure in the divertor chambers of ASDEX [17], all of which depended on the direction of the magnetic field. Nevertheless, it should be pointed out that comparing density peaks measured by DENSEPACK can be misleading since the highest density might have occurred in the top and bottom 40° gaps between probes. In any case this top-bottom variation was small compared to the dominant poloidal variation in density.

The poloidal variation of plasma density along the inside wall is presented with higher spatial resolution at a radius of 16.8 cm in Figure 4. The poloidal density gradient which appeared across only two probes in Figure 3 is shown to be smoothly varying over three or more data points. This verifies that the

density variation displayed previously was not due to a bad probe or some instrumental 'artifact'. It also verifies the relative calibration between probes. The absolute density maxima again appear to occur in the 40° probe gaps.

The poloidal asymmetry in density becomes more pronounced at larger minor radii. Figure 5 displays simultaneous poloidal density profiles at 250 msec for the three DENSEPACK radii of 16.8, 17.2, and 17.6 cm in a $\bar{n}_e \approx 1.8 \times 10^{14}/\text{cm}^3$, 200 kA, 8 tesla, hydrogen discharge. The density scales for the 17.2 and 17.6 cm radius data are multiplied by factors of 2 and 4 respectively for ease of comparison with the $r = 16.8$ cm data. The density measured by probes at $r = 17.6$ cm varies from a minimum of $\sim 7 \times 10^{10}/\text{cm}^3$ near the inside midplane (180°) to a maximum of $\sim 2 \times 10^{12}/\text{cm}^3$ near the top and bottom locations. This is at least a factor of 25 density variation in poloidal angle at this radius.

Figure 5 also shows that the poloidal locations of the density maxima are a function of minor radius although the exact locations of these maxima are not easy to discern with this probe spacing. At $r = 17.6$ cm, the maximum density data points appear to change location by $\approx 45^\circ$ relative to the 16.8 cm data points, moving toward the outside midplane. However, the absolute density maxima may have occurred in the two regions where there are no probes.

3.2 Temperature

The temperature profile in the SOL plasma was found to exhibit a poloidal variation similar to the density profile. Figure 6 shows a poloidal profile of electron temperature at 250 msec for the same discharge and minor radius position ($r = 16.8$ cm) which is displayed in Figure 3. These temperature data points were obtained by performing a 20 msec time-average of fitted temperatures.

One might expect that the temperature would exhibit a poloidal variation such that the plasma pressure remains relatively independent of angle. However, the reverse was found to be true. Poloidal positions of electron temperature maxima and minima coincided with the ' $-\cos(2\theta)$ ' dependence of the density maxima.

A minimum in the electron temperature was always detected at the small major radius edge of the plasma. Figure 6 indicates that the lowest temperature at this radius occurred near $\theta \approx 225^\circ$. It is interesting to note that this is the typical poloidal position where the MARFE phenomenon occurs in Alcator C. In fact, this discharge happened to display a MARFE at this location throughout the duration of the shot. Nevertheless, this poloidal structure in temperature still existed in discharges in which a MARFE did not occur. However, the minimum temperature in the non-MARFE case was not as low as ~ 5 eV at 16.8 cm as is displayed here.

The poloidal variation in electron temperature was never as dramatic as in the density case. Contrary to the density, the poloidal variation became less pronounced at larger minor radii. Figure 7 displays simultaneous poloidal electron temperature profiles at the three DENSEPACK radii. At 17.2 and 17.6 cm, most of this poloidal variation is within the experimental uncertainty, although there is a suggestion that the poloidal position of temperature maxima is a function of minor radius similar to the density maxima shown in Figure 5. In any case, the temperature was found to be a weak function of minor radius.

In some cases, the radial temperature profile appeared to invert. Data points at 315° in this figure show that the electron temperature increases in minor radius at this poloidal location. At first it was thought that there was a problem with the fitting algorithm or that one or two probes were mislabelled. Yet, no such problems were found, and this inverted temperature data remains a curiosity. However, in most other discharges this feature was not seen.

3.3 Pressure

Since the edge plasma density and electron temperature were found to be poloidally asymmetric, it follows that the electron pressure was asymmetric as well. The electron pressure (P_e) inferred from the density and temperature data in Figures 3 and 6 is plotted in Figure 8. The poloidal structure in pressure is determined mainly by the poloidal variation in density although the temperature variation adds to the asymmetry.

3.4 Density Scrape-off Length (λ_n)

With density at three radii being recorded simultaneously for a given shot, the density e-folding length (λ_n) as a function of poloidal angle could be inferred. Since the three radial measurements occurred at different poloidal angles, a linear interpolation scheme was used to estimate the radial density profile at a given angle. An exponential function was then fit to these points versus radius to yield a scrape-off length. Figure 9 displays the result of this procedure. Again, a clear poloidal structure appears, but with a different poloidal dependence.

While density and temperature data showed maxima near the top and bottom poloidal positions, this figure shows an overall scrape-off length maximum that is nearer to the outside. This is because the poloidal locations of the density maxima were found to be a function of minor radius. A factor of 3-8 variation in scrape-off length was typically recorded with the shortest scrape-off lengths occurring on the inside midplane (~ 0.1 cm). The poloidal structure of λ_n , in contrast to the plasma pressure, appeared to be more like ' $\cos\theta$ ' except for a slight relative minimum on the outside.

The scrape-off length is related to the balance of parallel and perpendicular particle fluxes in the SOL plasma. An accounting of these fluxes is often used to formulate a simple expression for λ_n in terms of the perpendicular diffusion coefficient (D_\perp) and sound speed flows (C_s) to the limiter ($\lambda_n \approx \sqrt{D_\perp L / C_s}$) [18]. Although the connection length to the limiter, L , changes from 125 cm at the outside midplane of the tokamak to 73 cm on the inside, this cannot account for the observed factor of 3-8 variation in λ_n .

A large poloidal variation in λ_n therefore suggests that the perpendicular transport processes which are active in the edge depend on poloidal location. The poloidal density and temperature profiles shown earlier suggested that this might be the case. However, the poloidal variation of the scrape-off length shown here more strongly supports this idea and is discussed in more detail in section 4.

3.5 Floating Potential

Independent of the density and temperature, the potential attained by an unbiased probe (floating potential) was recorded for a subset of probes in the DENSEPACK array. Figure 10 displays a poloidal profile of floating potential for probes at $r = 16.8$ cm. These data points represent a 30 msec time average at 250 msec into the discharge (time of constant plasma current). Once again, a well defined poloidal variation was recorded for this edge parameter. The floating potential was found to vary in poloidal angle like $-\sin\theta$, being negative at the bottom location and positive at the top. Typical extreme values at this radius were $\approx \pm 8$ to ± 15 volts. In addition, when the direction of the toroidal field was reversed, a $+\sin\theta$ -like dependence was observed (dotted line in Figure 10).

Unlike the density and temperature profiles shown previously, the overall poloidal structure in the floating potential can be simply explained at least to first order. The floating potential of a DENSEPACK probe relative to the limiter potential (taken as 0 volt reference by the electronics) is diagrammed in Figure 11. The limiter is a perturbing structure and sets the local value of the space or plasma potential (Φ_s) through the sheath drop to be roughly $\sim 3.5 T_e$ above the potential of the limiter. However, non-ambipolar transport mechanisms, such as $\underline{B} \times \nabla B$ particle drifts across the radial density gradient, can increase or decrease the space potential further away from the limiter surface. At the probe surface another sheath drop of $\sim 3.5 T_e$ occurs. The floating potential of the probe relative to the limiter therefore becomes

$$\Phi_f \approx \delta\Phi_s + 3.5 (T_e^{limiter} - T_e^{probe}) . \quad (1)$$

If T_e along a field line varies little so that $T_e^{probe} \approx T_e^{limiter}$, then $\Phi_f \approx \delta\Phi_s$, and the spatial variation in the floating potential should reflect the spatial variation in the plasma potential due to effects such as $\underline{B} \times \nabla B$ particle drifts.

For the normal magnetic field direction, the direction of the $\underline{B} \times \nabla B$ drift in Alcator C is from the bottom to the top of the poloidal cross-section. Thus, the potential variation, $\delta\Phi_s$, due to this charge separation depends on poloidal angle

as $-\sin\theta$. The magnitude of this potential variation near the limiter radius, a , for the case of circular flux surfaces with a poloidally uniform density e-folding length, λ_n , is [19],

$$\delta\Phi_s(\theta) \approx -8.3 \times 10^{-10} \frac{n Z_{eff} a^4 \Lambda B}{I_p^2 R_0 T_e^{1/2} \lambda_n} \sin\theta \quad (\text{volts}) \quad (2)$$

with plasma current, I_p , major radius, R_0 , and coulomb logarithm, Λ . Electron temperature, T_e , is in units of eV. All other quantities are in MKS units.

Using this equation with the parameters of Alcator C, one obtains potentials on the order $\sim \pm 8$ volts which is similar to the observed values. The observation of a change in sign of the floating potential variation corresponding to a change in the direction of \underline{B} is also consistent with this $\underline{B} \times \nabla B$ drift explanation.

The assumption that $T_e^{probe} \approx T_e^{limiter}$ along a field line is not expected to be satisfied in general. The departure of the measured floating potential from a pure $-\sin\theta$ variation may be a reflection of this fact. Discharges shown in Figure 10 were picked because they displayed the clearest $-\sin\theta$ structure. However, other discharges displayed a more distorted angular dependence of floating potential. This may be attributed to a non-negligible difference between the local probe and limiter electron temperatures.

3.6 Fluctuations

The DENSEPACK hardware was also configured to record high frequency fluctuations in the ion saturation current collected by 15 of the 30 active probes. Data from these probes was sampled at 1 MHz for 8 msec during the steady state portion of the discharge by fast data loggers. Spectral analysis techniques employing digital Fast Fourier Transforms (FFT) [20] were used with this data to infer fluctuation power spectra and to search for coherent modes extending over the plasma region between probes.

A. Power Spectrum

Figure 12 displays a typical power spectrum of ion saturation fluctuations from DENSEPACK probes. A numerical Gaussian filter in frequency with a half width of ≈ 1 kHz was used to smooth the spectrum. The spectrum displays no evidence of any clear modes localized in frequency with or without frequency smoothing. The fluctuations appear as a broad band ‘turbulence’ and exhibit a bandwidth and roll-off similar to the probe spectra obtained by Zweben [6]. The effect of a 416 kHz cutoff frequency lowpass filter inserted before the fast digitizer to eliminate aliasing is seen on the semi-log plot in Figure 12a at frequencies above 400 kHz. Data above ~ 450 kHz indicates the level of digital noise for this spectrum.

The power spectra could be characterized by the same parameters as those used by Zweben [21], namely, a critical frequency, f_{crit} , below which the power spectra were relatively flat and above which the power rolled off as $P(f) \propto f^{-\alpha}$. The exponent, α , was found to be in the range 1–3 for DENSEPACK data, similar to Zweben’s result. The ‘flat’ region also appeared similar to that found by Zweben. Typically, 80–85% of the fluctuation power was at frequencies below 50 kHz.

Power spectra obtained from probes at different poloidal locations were compared to search for a spatial dependence of the fluctuation spectrum. The spectrum was found to be very similar at all poloidal locations. The only notable difference from probe to probe was the rate of high frequency roll-off. For the same discharge, α was found to vary from ~ 1 to ~ 3 between probes. However, no systematic relationship between spatial position and α was detected.

B. Correlations

Crosscorrelations of probe signals and autocorrelations of a probe signal can be computed efficiently using Fourier transform techniques [22]. The correlation function was computed in this manner to obtain autocorrelation and crosscorrelation functions between 15 active probes on the DENSEPACK array.

A typical autocorrelation function deduced from an ion saturation current fluctuation power spectrum is plotted in Figure 13. The $\sin(at)/at$ structure in Figure 13a is due to wiggles in the low frequency end of the power spectrum. With more data samples, this feature disappears. Figure 13b shows this same autocorrelation on an expanded time scale. As shown here, it was found that typical autocorrelation times were on the order $\tau_{corr} \approx 10\text{--}20 \mu\text{sec}$.

Crosscorrelations of signals yielded no coherence even for adjacent probes except during a subset of shots where a MARFE was observed to move poloidally. This incoherence of the probe signals is consistent with the accepted spatial correlation length for fluctuations. From probe and electromagnetic scattering measurements [5], the power spectrum in perpendicular wavenumber, $P(k_\perp)$, peaks around $k_\perp \rho_s \approx 0.3$ where ρ_s is the ion Larmor radius evaluated at the electron temperature. For Alcator C edge plasma where $B \approx 8$ tesla and $T_e \approx 15$ eV, this implies a fluctuation correlation length of $\lambda_{corr} \approx 0.1$ cm. The closest DENSEPACK probe spacing was ~ 1 cm. Probes at the same minor radius location were spaced poloidally by ~ 3 cm (see Figure 2). Thus, it was not expected that there be any significant coherence in ion saturation fluctuations between probes on the DENSEPACK array.

One other way in which a coherence might be detected between probes is when the plasma has a bulk flow velocity directed from one probe to another. If the time for a volume of plasma to move from probe to probe is less than the autocorrelation time, τ_{corr} , then some degree of coherence would be displayed by the crosscorrelation function. With a probe spacing of ≈ 3 cm, this would necessitate a flow velocity of $V_\perp \approx 3 \times 10^5$ cm/sec. However, the estimated spatial correlation length for fluctuations of $\lambda_{corr} \approx 0.1$ cm implies that this velocity vector must align within 2° of a straight line path connecting two probes. Thus, it is unlikely that such a correlation between probes would be detected even if such a flow velocity in the edge plasma existed.

C. Spatial Variation of Fluctuation Amplitude

The fluctuation level in ion saturation current collected by probes, \tilde{J} , is most conveniently expressed relative to the time-averaged ion saturation current, \bar{J} , through the ratio \tilde{J}/\bar{J} . Here, and throughout the remainder of this paper, \tilde{J} is defined as the RMS fluctuation level about the mean of the ion saturation current. When electron temperature fluctuations are small, ion saturation current fluctuations are proportional to density fluctuations, allowing \tilde{J}/\bar{J} to be interpreted as \tilde{n}/\bar{n} .

\tilde{J}/\bar{J} was computed for ion saturation data recorded simultaneously by the 1 MHz and 10 kHz data loggers. The 10kHz digitizers had an analog bandwidth of ~ 50 kHz while the bandwidth of the fast, 1 MHz modules were limited only by the lowpass filters at 416 kHz. Figure 14 displays \tilde{J}/\bar{J} computed from both the 10 kHz and 1 MHz digitized data as a function of poloidal angle for two DENSEPACK radii of 16.8 cm and 17.2 cm. The 10 kHz digitized data represents an average of \tilde{J}/\bar{J} over the ion saturation portion of 16 Langmuir sweeps which spanned 80 msec during the steady state portion of the discharge. The 1 MHz digitized \tilde{J}/\bar{J} was computed from ~ 1000 points obtained during one of these 16 sweeps. The limited analog bandwidth of the 10 kHz digitized data ($100 \text{ Hz} \lesssim f \lesssim 50 \text{ kHz}$) relative to the 1 MHz digitized data ($100 \text{ Hz} \lesssim f \lesssim 416 \text{ kHz}$) is evident in Figure 14 as the former data points are typically 80–85% of the latter points. Ratios of \tilde{J}/\bar{J} computed from these two data sets were found to be insensitive to poloidal angle, consistent with the observation that the power spectrum itself was found to be independent of poloidal angle.

The data at 16.8 cm, shown in Figure 14a, was recorded with a better signal to noise level than the 17.2 cm data (Figure 14b) so that the error bars for this data are smaller. For both radii, there appears to be little or no systematic variation in the value of \tilde{J}/\bar{J} with poloidal angle. The 16.8 cm data does show some poloidal variation, suggesting that minima in \tilde{J}/\bar{J} may occur near the top and bottom poloidal locations. This may be a reflection of the high values of \tilde{J} recorded at these locations. However, this trend was not as readily observed in the 17.2 cm data where the relative fluctuation level was found to scatter about a mean value that was independent of poloidal angle.

4. Mechanisms Supporting Poloidal Asymmetry

The question of why the edge plasma should exhibit such a strong poloidal asymmetry naturally arises. This section explores four possible explanations for the measured asymmetry: 1) systematic errors in measurement due to incorrect installation of DENSEPACK and/or DENSEPACK perturbing the edge plasma, 2) noncircular magnetic flux surfaces, 3) spatially dependent perpendicular diffusion, and 4) spatially dependent perpendicular convection.

4.1 Check of Systematic Errors

A. DENSEPACK Installation

One possibility for the observed systematic variation in edge plasma parameters is that the DENSEPACK hardware was incorrectly installed. If the backbone structure of DENSEPACK was in fact elliptical, density and temperature differences on the same length probes would be detected.

The position of DENSEPACK was checked during a vacuum break midway through its operation. A fiber optic scope was inserted into the vacuum chamber to view the position of the backbone along the vacuum wall. It was found that the stainless steel ring segments were flush against the wall as designed. Therefore, DENSEPACK was indeed sampling plasma along concentric circles of radii 16.8, 17.2, and 17.6 cm.

The fact that the density scrape-off length was found to be a function of angle further verified that the edge plasma was truly asymmetric and that the DENSEPACK backbone was not displaced. No simple displacement in the probe array could account for the variation of the radial gradient measured by the experiment itself.

B. DENSEPACK Perturbations

Another possible way in which DENSEPACK could systematically cause a poloidal asymmetry to be detected was that the probe array itself perturbed the edge plasma. From Figure 2, one can see that there were no probes over a $\sim 40^\circ$ segment at the top and bottom locations. These were exactly the positions where plasma density and temperature maxima were found to exist. This raised concern that perhaps DENSEPACK, with its close-packed probes, was acting as a limiter and reducing the plasma density and temperature from the unperturbed values.

In order to test this hypothesis, the molybdenum casing of a gridded energy analyzer [23] was inserted in the top 40° gap between probes at the DENSEPACK port (C). Normally, the energy analyzer probe was pulled back and oriented with its length parallel to the magnetic field. For this test, it was rotated 90° to expose its maximum area to the plasma and act as a local 'limiter'. It was found that even when this 'limiter' was inserted to a radius of 16.7 cm, the poloidal profile of edge plasma parameters as inferred by DENSEPACK remained unchanged. The projected area of this 'limiter' (10° in poloidal extent) was much larger than the area of a DENSEPACK probe, and yet no perturbation in the edge parameters was detected. This was strong evidence to support the conclusion that DENSEPACK itself did not perturb the edge plasma in a way to cause the measured asymmetries.

An additional argument, similar to the one stated in the previous subsection, can be used. Even if DENSEPACK was perturbing the edge plasma, the poloidal variation in the scrape-off length could not be simply explained. It is not likely that the same physical arrangement of probes on the inside and outside positions of the torus would lead to dramatically different gradients in the radial density profile. It was therefore concluded that poloidal asymmetries detected by DENSEPACK were due to true asymmetries appearing in the limiter shadow plasma of Alcator C.

4.2 Magnetic Flux Surfaces

Perhaps the simplest explanation for the observed poloidal pressure asymmetries is that the outer magnetic flux surfaces in Alcator C were not circular and did not align with the limiters. In order to examine this possibility, a system of twelve poloidal flux loops positioned just outside the vacuum vessel was used to infer the outer magnetic flux surface shape in Alcator C [24]. A direct comparison of density and temperature data obtained by DENSEPACK with measurements of outer magnetic flux surface shape was therefore made.

In order to facilitate this comparison of flux surface shape with measured edge plasma parameters, DENSEPACK data and magnetic flux data were similarly processed to yield contour plots of constant electron pressure ($P_e = n \times T_e$) and magnetic flux for the same discharge. Since the ion temperature was expected to roughly follow the electron temperature (measurements show that typically $T_i \approx 1-3 T_e$ [23]), variations in total plasma pressure were expected to follow variations in P_e , enabling a test of the constant pressure surface hypothesis. The following two subsections present the details of this comparison.

A. Poloidal Contours of Constant $\text{Log}(P_e)$

The DENSEPACK probe array samples plasma in a thin annular region in the SOL plasma as shown in Figure 15a. In order to view contours of constant edge plasma parameters plotted on this poloidal cross-section, it is more convenient to artificially expand the radial dimension leading to a 'conformal mapping' as shown in Figure 15b. This mapping effectively places the radius $r = 15.7$ cm at the center of the plot and $r = 17.6$ cm at the outer edge.

Contours of constant logarithm of electron pressure are plotted in this format in Figure 16a. This logarithmic plot directly displays the poloidal variation in pressure scrape-off length since the spacing between the contours is proportional to the e-folding length. As shown previously, the density or pressure scrape-off length is longer on the outside than on the inside midplane.

B. Constant Flux Contour Plots

In the SOL plasma, where negligible current flows compared to the central plasma current, Maxwell's equations in vacuum can be used to interpolate for the magnetic field between the poloidal flux loops up to the limiter radius. Outer flux surfaces resulting from this procedure are plotted in figure 16b.

The magnetic flux and electron pressure surfaces (P_e) shown in Figure 16 clearly show that pressure is not constant on a flux surface in the limiter shadow plasma. The flux surfaces show only a minor distortion from circular whereas the pressure plot is far from circular. The most dramatic departure from $P = \text{const.}$ is at large minor radii. A flux contour near the maximum radii sampled by DENSEPACK traverses many pressure contour lines as it encircles the plasma. The variation in electron pressure along these contours easily exceeds a pressure ratio of 50:1.

Even when the plasma position was moved in-out or up-down so that the outer flux surfaces shifted relative to the surfaces shown in Figure 16b, the picture in Figure 16 still held true. Although in these cases the pressure surfaces shifted slightly, it was found that the pressure profiles consistently violated $P = \text{const.}$ on a flux surface and exhibited the same poloidally asymmetric structure.

The conclusion drawn from this data was that there were processes active in the limiter shadow plasma to support strong poloidal pressure asymmetries on a flux surface in violation of the often assumed model. This is not so surprising in view of the fact that MARFEs were found early in the operation of Alcator C to be toroidally symmetric, independent of the rotational transform.

4.3 Spatially Dependent Diffusion

There are a number of mechanisms which could explain the observed density and temperature asymmetries on a flux surface in the SOL plasma. One possibility is that plasma transport processes are a function of space. Alternatively or in addition, plasma sources and sinks could be spatially non-uniform.

The radiation term in the electron energy equation is an example of such a local sink which can disturb the electron temperature profile and possibly lead to a radiation thermal instability (MARFE). The continuity equation, which provides an accounting of the local plasma density, also includes an ionization source term and recombination sink term.

Since the most marked poloidal asymmetry occurs in the density profile, the continuity equation merits the most immediate attention. For typical edge plasma temperatures of 5–20 eV, recombination is negligible. With the short parallel connection length, $L \approx 100$ cm, ionization can also be neglected in the SOL plasma of Alcator C. Thus, neutrals and the associated source and sink terms in the continuity equation can be ignored. The only dominant terms remaining are diffusion and convection.

Fortunately, for typical Alcator C edge densities, $n \approx 10^{13}$ – 10^{14} /cm³, and temperatures, $T_e \approx 5$ –20 eV, the SOL plasma is sufficiently collisional to be treated as an MHD fluid [25–27]. Consequently, diffusion and convection terms can be easily examined within the framework of this relatively simple model. This subsection uses the MHD fluid description to examine spatially dependent perpendicular diffusion as a possible mechanism to explain the observed poloidal density asymmetry. The following subsection uses a similar approach to address the issue of poloidally asymmetric perpendicular convection.

A. Scrape-off Length Variation: Spatially Dependent Diffusion

The first complication that one may consider in modelling transport in the limiter shadow plasma is that the cross-field diffusion rate is some function of space. In the model considered here, plasma is convected to limiter surfaces along field lines, and the plasma density is assumed to be approximately toroidally symmetric, $\frac{\partial}{\partial \phi} \rightarrow 0$. However, the perpendicular flux due to diffusion is written with a poloidal dependence as

$$\Gamma_{\perp} = -D_{\perp}(\theta) \nabla_{\perp} n = -D_{\perp}(\theta) \left[\frac{\partial n}{\partial r} \hat{r} + \frac{B_{\phi}^2}{B^2 r} \frac{\partial n}{\partial \theta} \hat{\theta} \right]. \quad (3)$$

where a cylindrical (r, θ, ϕ) coordinate system is used. The continuity equation can therefore be written as

$$\nabla \cdot \underline{\Gamma}_{\perp} = -\nabla \cdot \underline{\Gamma}_{\parallel} \quad (4)$$

$$-D_{\perp}(\theta) \frac{\partial^2 n}{\partial r^2} - \frac{1}{r} \frac{\partial}{\partial \theta} \left[D_{\perp}(\theta) \frac{B_{\phi}^2}{B^2} \frac{1}{r} \frac{\partial n}{\partial \theta} \right] \approx -\frac{n C_s}{L(\theta)} \quad (5)$$

where the divergence of the parallel flow to the limiter is approximated as the local loss rate to the limiters. The fact that the parallel connection length, $L(\theta)$, depends on poloidal angle is explicitly shown for clarity. Since radial derivatives dominate, Equation 5 reduces to

$$D_{\perp}(\theta) \frac{\partial^2 n}{\partial r^2} \approx \frac{n C_s}{L(\theta)} \quad (6)$$

A poloidal density profile at the limiter radius, $n_a(\theta)$, and a density of zero at $r \rightarrow \infty$ can be specified as the boundary conditions so that

$$n(r, \theta) = n_a(\theta) e^{(a-r)/\lambda_n(\theta)} \quad (7)$$

which yields

$$\lambda_n(\theta) = \sqrt{\frac{L(\theta) D_{\perp}(\theta)}{C_s}} \quad (8)$$

Thus, the first order response of the SOL plasma to a poloidally dependent perpendicular diffusion coefficient is a local adjustment of the radial scrape-off length. The density at the limiter radius is not directly determined by D_{\perp} but is obtained by matching the fluxes crossing from the central plasma into the SOL plasma. Consequently, poloidal variations in density offer no unambiguous

information about D_{\perp} . However, λ_n is readily determined from DENSEPACK data and can be directly related to D_{\perp} through Equation 8.

The poloidal variation of 3–8 in scrape-off length detected by DENSEPACK implies a 5–30 variation in D_{\perp} , even when allowing a factor of ~ 2 variation in $L(\theta)$. Furthermore, including poloidal diffusion terms in Equation 6 could only result in a reduction of the poloidal variation of the plasma density. Thus, a factor of 5–30 variation in D_{\perp} represents the minimum variation required to explain the poloidal variation in λ_n .

Since the anomalous level of D_{\perp} observed in the edge plasma of tokamaks is often ascribed to turbulence, one would expect that a factor of 5–30 variation in D_{\perp} would show up as some variation in the fluctuation level characterized by \tilde{J}/\bar{J} . However, as discussed in section 3.6, no clear evidence of any systematic poloidal variation in \tilde{J}/\bar{J} was found. The conclusion is that either D_{\perp} changes in space independent of the relative power in the fluctuations characterized by \tilde{J}/\bar{J} or that some other mechanism is responsible for the poloidal asymmetries. This apparent inconsistency prompts the following discussions of other mechanisms which could cause the edge density profile to be asymmetric.

B. Scrape-off Length Variation: Directed \tilde{n} , $\tilde{\Phi}_s$ Fluxes

Another possible cause of the scrape-off length variation is that edge plasma turbulence in Alcator C does not lead to a purely isotropic diffusion flux but rather a directed, time-averaged $\langle \tilde{n} \tilde{\underline{E}} \times \underline{B} \rangle$ flux. In this case, the level of \tilde{J}/\bar{J} is not important in determining the magnitude of the perpendicular flux. Instead, the relative phase of density fluctuations, \tilde{n} , and gradients in space potential fluctuations, $\nabla_{\perp} \tilde{\Phi}_s$, determines the magnitude and direction of this time-averaged flux. Such fluctuation-induced particle fluxes due to \tilde{n} and $\tilde{\Phi}_s$ have been detected in the edge plasma of other tokamaks [6,7].

A possible scenario which could explain the measured poloidal variation in the density profile is that coherent components of \tilde{n} , $\tilde{\Phi}_s$ fluctuations are phased

differently at various poloidal angles in the edge plasma. These fluctuation induced particle fluxes can then add or subtract to the local, purely diffusive flux, depending on the poloidal position.

More formally, one can divide the perpendicular fluxes into two components: a part that includes an isotropic diffusion and a part that results from phase correlated $\tilde{n}, \tilde{\Phi}_s$ fluctuations [28],

$$\Gamma_{\perp} = \Gamma_{\perp}^D + \Gamma_{\perp}^{\tilde{n}, \tilde{\Phi}} \quad (9)$$

$$\Gamma_{\perp}^D = D_{\perp} \nabla_{\perp} n \quad (10)$$

$$\Gamma_{\perp}^{\tilde{n}, \tilde{\Phi}} = \int \frac{\tilde{n}(\omega) \underline{B} \times \nabla \tilde{\Phi}_s(\omega)}{B^2} \cos \gamma(\omega) \partial \omega, \quad (11)$$

with $\gamma(\omega)$ defined as the phase angle between these two fluctuating quantities. Here, the directed turbulent flux is assumed to be dependent on poloidal angle. On the other hand, D_{\perp} is no longer assumed to be a function of space. Incorporating $\Gamma_{\perp}^{\tilde{n}, \tilde{\Phi}}$ into Equation 6 yields a new version of Equation 8,

$$\lambda_n(\theta) = \sqrt{\frac{D_{\perp}}{C_s/L(\theta) - S^{\tilde{n}, \tilde{\Phi}}(\theta)}}, \quad (12)$$

where

$$S^{\tilde{n}, \tilde{\Phi}}(\theta) = - \int \left[\frac{\underline{B} \times \nabla \tilde{\Phi}_s(\omega)}{B^2} \right] \cdot \frac{\nabla \tilde{n}(\omega)}{\bar{n}} \cos \gamma(\omega) \partial \omega \quad (13)$$

and \bar{n} is defined as the time-averaged density.

Thus, the density scrape-off length depends on the relative sign and magnitude of $S^{\tilde{n}, \tilde{\Phi}}$ compared to C_s/L . In view of the fact that potential and density

fluctuations occur over very short spatial correlation lengths (~ 0.1 cm for Alcator C), it is possible that $S^{\tilde{n}, \tilde{\Phi}}$ can be large enough to explain the observed density asymmetry. Ideally, one needs to simultaneously measure $\nabla \tilde{n}/\bar{n}$ and $\nabla \tilde{\Phi}_s$ at various poloidal locations in order to compute $S^{\tilde{n}, \tilde{\Phi}}$. Unfortunately, no simultaneous measurements of $\nabla \tilde{n}/\bar{n}$ and $\nabla \tilde{\Phi}_s$ have been made in Alcator C edge plasma.

4.4 Perpendicular Convection

In addition to fluctuations in plasma density and potential, the edge plasma exhibits non-zero time-averaged components of n and Φ_s . The fact that the edge plasma can maintain near steady state gradients in Φ_s prompts one to consider the impact that $\underline{E} \times \underline{B}$ bulk plasma flows may have on the equilibrium density profile.

In principle, it is possible to infer 2-D $\underline{E} \times \underline{B}$ flow patterns directly from DENSEPACK data. From these flow patterns and the already inferred 2-D density profile, the impact of this perpendicular convection can be evaluated. Alternatively, one can estimate directly the magnitude and structure of the perpendicular convection flow pattern that would be needed to account for the observed density asymmetry. Both these approaches were used with DENSEPACK data and are now discussed.

A. Perpendicular Convection Transport Terms

The continuity equation can be expressed as,

$$\nabla \cdot \underline{\Gamma}^D + \underline{V}^C \cdot \nabla n + n \nabla \cdot \underline{V}^C = 0 \quad (14)$$

where $\underline{\Gamma}^D$ is the particle flux due to diffusion, and \underline{V}^C is some convection velocity.

Perpendicular convection in Equation 14 is assumed to arise from $\underline{E} \times \underline{B}$ and diamagnetic particle drifts. From the MHD description,

$$\underline{V}_\perp^C = \frac{\underline{B} \times \nabla \Phi_s}{B^2} + \frac{\underline{B} \times \nabla P_i}{q n B^2} \quad (15)$$

where \underline{E} is written as $-\nabla \Phi_s$ with Φ_s and P_i being the local plasma potential and ion pressure respectively.

The bulk plasma accelerates to the sound speed along field lines as it approaches the limiter surface. This effect leads to a local plasma sink term in the continuity equation of order

$$\nabla_\parallel \cdot n \underline{V}_\parallel^C \approx \frac{n C_s}{L} \quad (16)$$

DENSEPACK data shows that radial density profiles in the limiter shadow plasma are modelled well by Equation 7. Assuming that D_\perp , T_i , and T_e are only weak functions of space, and using the fact that radial gradients are much larger than poloidal gradients, the continuity equation can be approximated as

$$-\frac{D_\perp n}{\lambda_n^2(\theta)} + \left[\frac{\underline{B} \times \nabla \Phi_s}{B^2} \right] \cdot \nabla n \approx -\frac{n C_s}{L} \quad (17)$$

since it can be shown from Equation 15 that $\nabla \cdot \underline{V}^C = -\mu_0 \underline{E} \cdot \underline{J} / B^2 \approx 0$ in the SOL plasma.

The impact of $\underline{E} \times \underline{B}$ convection on the density profile in the limiter shadow plasma can now be seen from Equation 17. In the absence of an $\underline{E} \times \underline{B}$ convection, this equation reproduces the unperturbed exponential density profile. Therefore, in order for the perpendicular convection term to significantly perturb the density profile, it must be the same order of magnitude as other terms in this equation. Using the local sink term in this equation as a comparison, this requirement is that

$$|\epsilon_n| \approx 0.1-1 \quad (18)$$

where

$$\epsilon_n \equiv \frac{L \left[\frac{\underline{B} \times \nabla \Phi_s}{B^2} \right] \cdot \nabla n}{n C_s} \quad (19)$$

Finally, λ_n can be estimated in terms of ϵ_n from Equation 17,

$$\lambda_n(\theta) = \frac{\lambda_{n0}(\theta)}{\sqrt{1 + \epsilon_n(\theta)}}, \quad (20)$$

where $\lambda_{n0}(\theta)$ is defined as the scrape-off length for the case no convection with poloidally symmetric diffusion, $\lambda_{n0}(\theta) = \sqrt{D_{\perp} L(\theta) / C_s}$. Thus, perpendicular convection is another process which can result in a density scrape-off length that depends on angle. Should ϵ_n approach -1 , a very long scrape-off length would result. On the other hand, if ϵ_n is $+1$, the scrape-off length becomes a factor of $1/\sqrt{2}$ shorter.

B. Magnitude of Perpendicular Convection Terms from $\nabla \Phi_s$ Data

A conformal contour plot of floating potential in the SOL plasma (Φ_f) is shown in Figure 17a. No spatial smoothing is performed on this data. However, a 40 msec time-average is applied to reduce the statistical error from fluctuations.

This figure illustrates that in the SOL plasma, where field lines intercept a grounded limiter surface, a steady state floating potential variation is maintained by some process. The overall floating potential variation can be explained in terms of $\underline{B} \times \nabla B$ particle drifts across a pressure gradient (section 3.5). The detailed structure appears to be related to temperature variations although other processes such as local non-ambipolar perpendicular transport cannot be disregarded.

The local plasma space potential (Φ_s) can be obtained from the electron temperature and floating potential. Relative to the limiter potential (defined as 0 volt reference), the local space potential is approximated as

$$\Phi_s \approx \Phi_f + 3.5 T_e . \quad (21)$$

Figure 17b shows poloidal contours of constant space potential. Here, smoothing in both angle and radius is performed.

Once $\Phi_s(r, \theta)$ is obtained from DENSEPACK data, the perpendicular $\underline{E} \times \underline{B}$ velocity due to space potential variations can be computed using Equation 15. Since \underline{V}_\perp^C is perpendicular to both \underline{B} and $\nabla\Phi_s$, and \underline{B} is mostly toroidal, the $\underline{E} \times \underline{B}$ flow field closely follows surfaces of constant Φ_s .

ϵ_n obtained from the inferred \underline{V}_\perp^C and the measured density gradients, is plotted in Figure 18. Typical values of ϵ_n range from -0.15 to $+0.15$. This indicates that perpendicular convective particle transport in the shadow plasma is indeed significant enough not to be ignored. However, as indicated from both the poloidal variation and magnitude of ϵ_n , this convection does not readily explain the observed poloidal density asymmetry.

From Equation 20, a variation of ϵ_n from -0.15 to $+0.15$ implies a scrape-off length variation of only $\approx 15\%$. In addition, the areas of positive ϵ_n and negative ϵ_n do not coincide with the poloidal variation of the scrape-off length or density. Therefore, it is concluded from this simple model that although perpendicular convective particle transport can perturb the edge density profile, it cannot directly explain the observed poloidal asymmetry in density.

C. Scrape-off Length Variation: Spatially Dependent Convection

One problem with the above approach is that it relies on the accuracy of measured gradients in density and temperature. Because of the factor of ~ 3.5 in Equation 21, the space potential is dominated by the electron temperature. The accuracy of the space potential is thus no better than the accuracy of the inferred electron temperature. Not only are the magnitudes important but the directions of the $\nabla\Phi_s$ and ∇n are as well, since a dot product must be performed in Equation 19. Another approach is to estimate the magnitude and

poloidal structure of the perpendicular convection flow pattern that would be needed to account for the observed asymmetries.

ϵ_n can be separated into poloidal and radial parts,

$$\epsilon_n = \frac{V_\theta \cdot \nabla_\theta n}{n C_s} L + \frac{V_r \cdot \nabla_r n}{n C_s} L. \quad (22)$$

The measured scrape-off length variation can be modelled as

$$\lambda_n(\theta) \approx \lambda_{n0} + \lambda_{n1} \cos\theta \quad (23)$$

where $\lambda_{n0} \approx 0.4$ cm and $\lambda_{n1} \approx 0.25$ cm for the data shown in Figure 9.

The scrape-off length maxima and minima occur near the outside and inside midplane locations, respectively. This implies that ϵ_n must be uniformly negative over the outside half of the poloidal cross-section and uniformly positive over the inside half of the poloidal cross-section in order to account for the overall variation in λ_n . However, at the inside and outside-midplane locations, the poloidal density gradient is near zero and changing sign since minima in density occur there. Consequently, the poloidal convection part of Equation 22 cannot provide the required poloidal variation in ϵ_n . Our attention therefore turns to the radial part of Equation 22.

From Equations 20 and 22, the poloidal variation in radial convection velocity, V_r , needed to explain the variation in λ_n modelled by Equation 23 is

$$V_r(\theta) = \frac{C_s \lambda_{n1} \cos\theta (2 \lambda_{n0} + \lambda_{n1} \cos\theta)}{L (\lambda_{n0} + \lambda_{n1} \cos\theta)}. \quad (24)$$

At the extrema, $V_r(\theta)$ becomes,

$$V_r^{max} \approx .004 C_s \approx 1.6 \times 10^4 \text{ cm/sec} \quad (25)$$

$$V_r^{min} \approx -.009 C_s \approx -3.7 \times 10^4 \text{ cm/sec} . \quad (26)$$

The poloidal electric fields for the $\underline{E} \times \underline{B}$ velocity implied by Equations 25 and 26 are on the order $E_\theta \approx \pm 20$ volts/cm. This is much higher than the $E_\theta \approx \pm 2$ volts/cm potential variations inferred by DENSEPACK (Figure 17b).

In summary, the analysis of DENSEPACK $\nabla \Phi_s$ data outlined in this subsection indicates that although $\underline{E} \times \underline{B}$ particle transport in the SOL plasma can be significant compared to the loss rate of particles to the limiter, it is not sufficient to explain the observed poloidal density asymmetry in any clearcut manner. Conversely, the convection flow pattern that is needed to explain the scrape-off length asymmetry implies potential variations that are higher than those inferred from the DENSEPACK probe array. Therefore, unless the potentials obtained from Equation 21 are grossly in error, it is not likely that near steady state $\underline{E} \times \underline{B}$ fluxes cause the observed scrape-off length asymmetry in the SOL plasma of Alcator C.

5. Poloidal Asymmetries Inside the Limiter Radius

The above analysis of perpendicular transport processes is restricted to the SOL plasma sampled by DENSEPACK. However, there is strong evidence that poloidal asymmetries are not restricted to this region and can appear on closed flux surfaces inside the limiter radius.

From the density profiles and scrape-off lengths measured by DENSEPACK, the poloidal variation in the density profile can be extrapolated to the limiter radius. Figure 19 shows a typical density profile at $r = 16.5$ cm (limiter radius) from this procedure. Note that even at the limiter radius, the density retains the same asymmetric structure and exhibits at least a factor of 2 variation over poloidal angle. Note also that the density maxima are shifted to the small major radius side of the top and bottom locations. The values of these maxima are very large at $n_e \approx 10^{14}/\text{cm}^3$ compared to the central line-averaged density,

$\bar{n}_e \approx 2 \times 10^{14}/\text{cm}^3$. Thus, the edge plasma just inside the limiter radius must also support strong poloidal asymmetries.

The asymmetries detected during MARFE phenomena are consistent with these observations from DENSEPACK. At the onset of a MARFE, a buildup of density is typically detected at the smaller major radius edge of tokamak plasmas by density interferometer measurements [8-11,13]. In Alcator C, the line-averaged density along the inside vertical chord can approach or exceed the central line-averaged density [13]. Relating the path of this inside interferometer beam (-12 cm inside the magnetic axis) to the poloidal density profile at the limiter radius shown in Figure 19, one can see that it passes through high density and steep poloidal density gradient plasma (dashed lines in figure 19). However, the line-integral of this density in the SOL plasma is not nearly enough to account for the observed density buildup along this chord. Consequently, the density asymmetry must not only extend inside the limiter radius, $r \lesssim a$, but also be more pronounced there.

The radiating MARFE region coincident with these events is observed to be strictly toroidally symmetric, not following field lines. Furthermore, this radiating region is found to extend slightly inside the limiter radius where field lines are not intercepted by limiter surfaces [9]. This is further evidence of a poloidally asymmetric plasma existing on closed fluxes surfaces inside the limiter radius.

The implication of these observations combined with DENSEPACK data is that perpendicular transport in both the SOL and a small annular region inside the limiter radius is highly poloidally asymmetric. Gradients are thereby supported along field lines. The resulting picture is an edge plasma that displays poloidal asymmetries yet retains toroidal symmetry.

Transport modelling of the edge plasma region just inside the limiter radius is more complex than the SOL plasma. One must now include neutral ionization source terms which could be neglected in the SOL of Alcator C. In addition, steady state $\underline{E} \times \underline{B}$ fluxes may be more important. The poloidal limiter which was present during the DENSEPACK experiment is not available to 'short out' E-fields in this region.

Unfortunately, this plasma region is difficult to diagnose. Nevertheless, the transport processes in this region result in a poloidally asymmetric density boundary condition for the SOL plasma.

6. Summary

The limiter shadow plasma of Alcator C as diagnosed by a poloidal array of Langmuir probes, DENSEPACK, is described. Marked poloidal asymmetries in density, density scrape-off length, electron temperature, and floating potential are found independent of central plasma parameters or the onset of MARFE conditions. These poloidal asymmetries show that pressure is not constant on a flux surface in the SOL plasma.

The possibility of poloidally asymmetric diffusion and/or convection supporting these measured asymmetries is examined. Fluctuation measurements do not suggest that turbulent diffusion is spatially dependent. On the other hand, it is pointed out that time-averaged \tilde{n} , $\tilde{\Phi}_s$ fluxes which cannot be quantified in this experiment may contribute to the asymmetry. On a longer time scale ($\tau \approx 5$ msec), $\underline{E} \times \underline{B}$ convection is computed from space potential variations inferred by DENSEPACK. It is found that although near steady state E-fields can significantly perturb the density profile, they do not readily explain the poloidally asymmetric scrape-off plasma. Conversely, the convection pattern which is needed to explain the asymmetry necessitates E-fields which are not detected by DENSEPACK. Therefore, lacking any clear-cut explanation for the measured asymmetries in terms of these measured quantities, \tilde{n} , $\tilde{\Phi}_s$ fluctuations are identified as the most likely mechanism that drives poloidally asymmetric transport. Unfortunately, no data exists on the Alcator C tokamak at this time to support or refute this hypothesis.

Poloidal density profiles extrapolated to the limiter radius indicate that poloidal asymmetries and associated asymmetric perpendicular transport processes are present inside the limiter radius as well. Observations of MARFE phenomena support this hypothesis and imply that asymmetric perpendicular

transport dominates in a small annular plasma region, just inside the limiter radius. The result of this strong perpendicular transport is a poloidally asymmetric yet toroidally symmetric edge plasma. Finally, it is recognized that near steady state $\underline{E} \times \underline{B}$ convection may play a more dominant role in this region of Alcator C where metallic limiters do not 'short out' systematic potential variations on a magnetic flux surface.

Acknowledgements

The authors gratefully acknowledge the Alcator C operations research group and support staff for their assistance in the collection of this data. Special thanks are extended to Pat Pribyl for measurements and analysis of poloidal flux data.

References

- [1] Wagner, F., Keilhacker, M., and the ASDEX and NI Teams, *J. Nucl. Mat.* **121** (1984) 103.
- [2] Nagami, M., Kasai, M., Kitsunozaki, A., Kobayashi, T., Konoshima, S., *et al.*, *Nucl. Fus.* **24** (1984) 183.
- [3] Kaye, S. M., Bell, M.G., Bol, K., Boyd, D., Brau, K., *et al.*, *J. Nucl. Mat.* **121** (1984) 115.
- [4] Staib, P., *J. Nucl. Mat.* **111 & 112** (1982) 109.
- [5] Liewer, P. C., *Nucl. Fus.* **25** (1985) 543.
- [6] Zweben, S. J., Liewer, P. C., Gould, R. W., *J. Nucl. Mat.* **111 & 112** (1982) 39.
- [7] Ritz, Ch.P., Bengston, R. D., Levinson, S.J., Powers, E.J., *Phys. Fluids* **27** (1984) 2956.
- [8] Baker, D. R., Snider, R. T., Nagami, M., "Observation of Cold, High-Density Plasma Near the Doublet III Limiter," General Atomic Rep. GA-A16337 (1981).
- [9] Lipschultz, B., LaBombard, B., Marmar, E. S., Pickrell, M. M., Terry, J. L., Watterson, R., Wolfe, S. M., *Nucl. Fus.* **24** (1984) 977.
- [10] Alladio, F., Bartiromo, R., Casali, B., Buratti, P., De Marco, F., *et al.*, *Phys. Let.* **90A** (1982) 405.
- [11] O'Rourke, J., Campbell, D., Denne, B., Gondhalekar, A., Gottardi, N., *et al.*, in Conference on Controlled Fusion and Plasma Physics (Proc. 12th Eur. Conf. Budapest, 1985) Vol. 9F, Part I, 155.
- [12] Boody, F.P., Bush, C.E., Medley, S.S., Park, H., Schivell, J., "Macroscopic Edge Phenomena in TFTR: MARFES, Moving MARFES, and Detached Plasmas," *Bull. Amer. Phys. Soc.* **30** (1985) 1518.
- [13] LaBombard, B., "Poloidal Asymmetries in the Limiter Shadow Plasma of the Alcator C Tokamak," M.I.T. Plasma Fusion Center Rep. PFC/RR-86-6 (1986).

- [14] LaBombard, B., Lipschultz, B., "DENSEPACK: A Poloidal Array of Langmuir Probes in the Limiter Shadow Plasma of the Alcator C Tokamak," M.I.T. Plasma Fusion Center Rep. PFC/JA-85-42 (1985).
- [15] Terry, J.L., Marmor, E.S., Chen, K.I., *Phys. Rev. Lett.* **39** (1977) 1615.
- [16] Brau, K., Suckewer, S., Wong, S.K., *Nucl. Fus.* **23** (1983) 1657.
- [17] Fussmann, G., Poschenrieder, W., Bernhardt, K., Richter, B., Szymansky, Z., and the ASDEX and NI Teams *J. Nucl. Mat.* **121** (1984) 164.
- [18] Uehara, K., Gomay, Y., Yamamoto, T., Suzuki, N., Maeno, M., Hirayama, T., Shimada, M., Konoshima, S., Fujisawa, N., *Plasma Physics* **21** (1979) 89.
- [19] LaBombard, B., "Comments on Equilibrium Plasma Flows in the Limiter Shadow Region of Alcator C," M.I.T. Plasma Fusion Center Rep. PFC/RR-83-26 (1983).
- [20] Brigham, E.O., *The Fast Fourier Transform*, Prentice-Hall, Inc., Englewood Cliffs, N.J., (1974).
- [21] Zweben, S. J., Gould, R. W., *Nucl. Fusion* **23** (1983) 1625.
- [22] Hooper, E. B., *Plasma Physics* **13** (1971) 1.
- [23] Wan, A. S., Yang, T. F., Parker, R. R., "A Localized Directional Edge Plasma Diagnostic on Alcator C," *Bull. Amer. Phys. Soc.* **29** (1984) 1223.
- [24] Pribyl, P., "Measured MHD Equilibrium in Alcator C," M.I.T. Plasma Fusion Center Rep. PFC/RR-86-7 (1986).
- [25] Freidberg, J. P., *Rev. Mod. Phys.* **54** (1982) 801.
- [26] Singer, C. E., Langer, W. D., "Axisymmetric Tokamak Scrapeoff Transport," Princeton Plasma Physics Lab. Rep. PPPL-1920 (1982).
- [27] LaBombard, B., "Reduced Fluid Transport Equations for the Edge Plasma of the Alcator C Tokamak," M.I.T. Plasma Fusion Center Rep. PFC/RR-86-9 (1986).
- [28] Liewer, P.C, McChesney, J.M., Zweben, S.J., Gould, R.W., *Phys. Fluids* **29** (1986) 309.

Figure 1 - Top view of the DENSEPACK probe array and limiter configuration in the Alcator C tokamak. Pairs of full and partial poloidal ring limiters occupy *B* and *E* access ports, thereby 'scraping off' the SOL plasma sampled by DENSEPACK ('C' port) with poloidal uniformity.

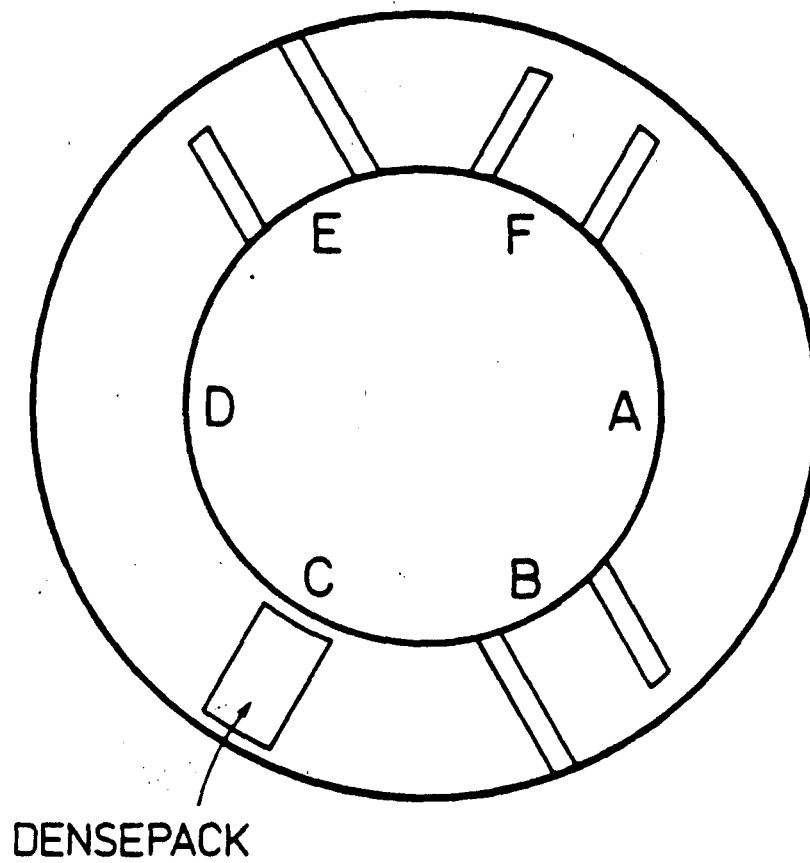
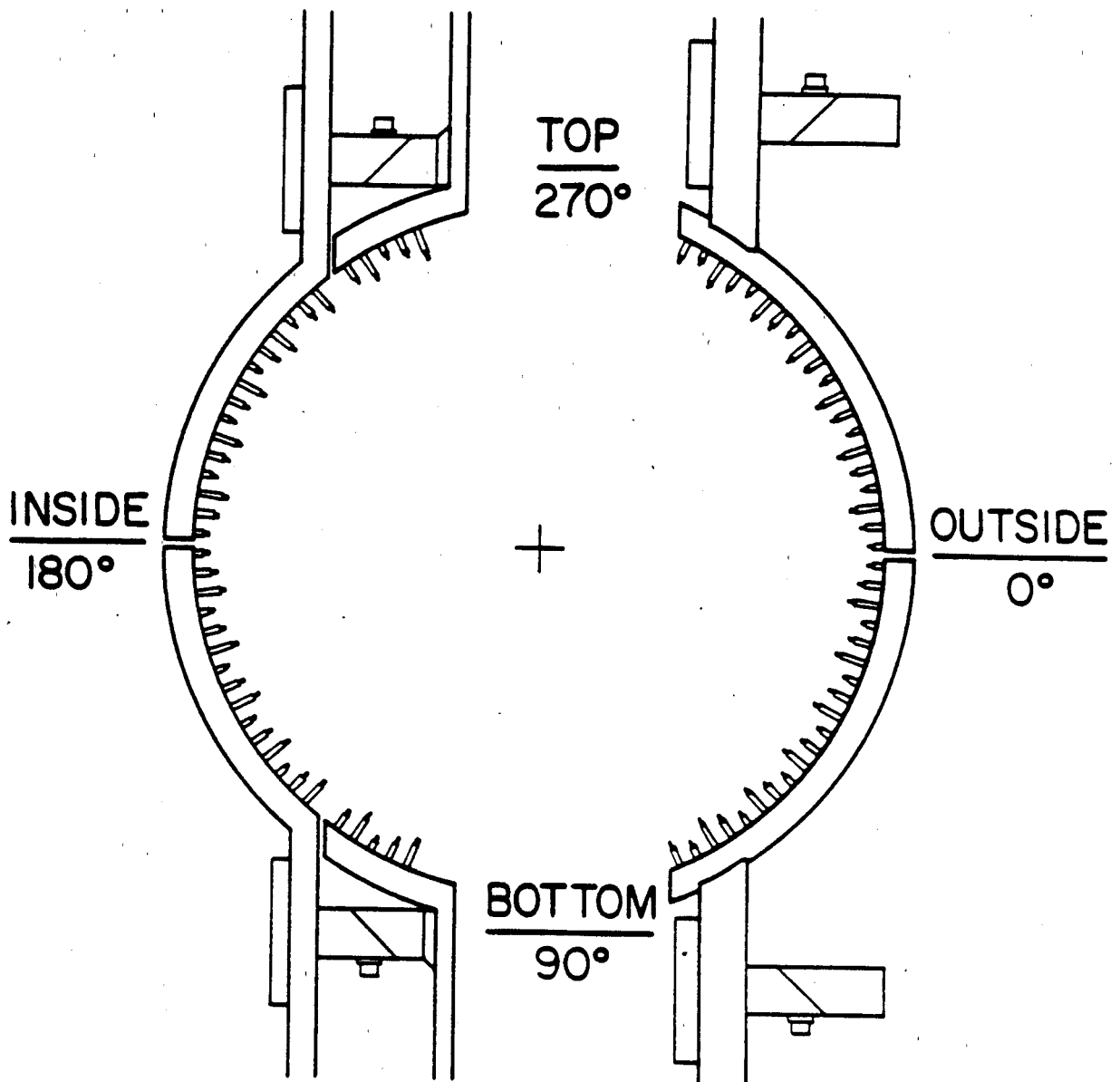


Figure 1

8/03/19/13

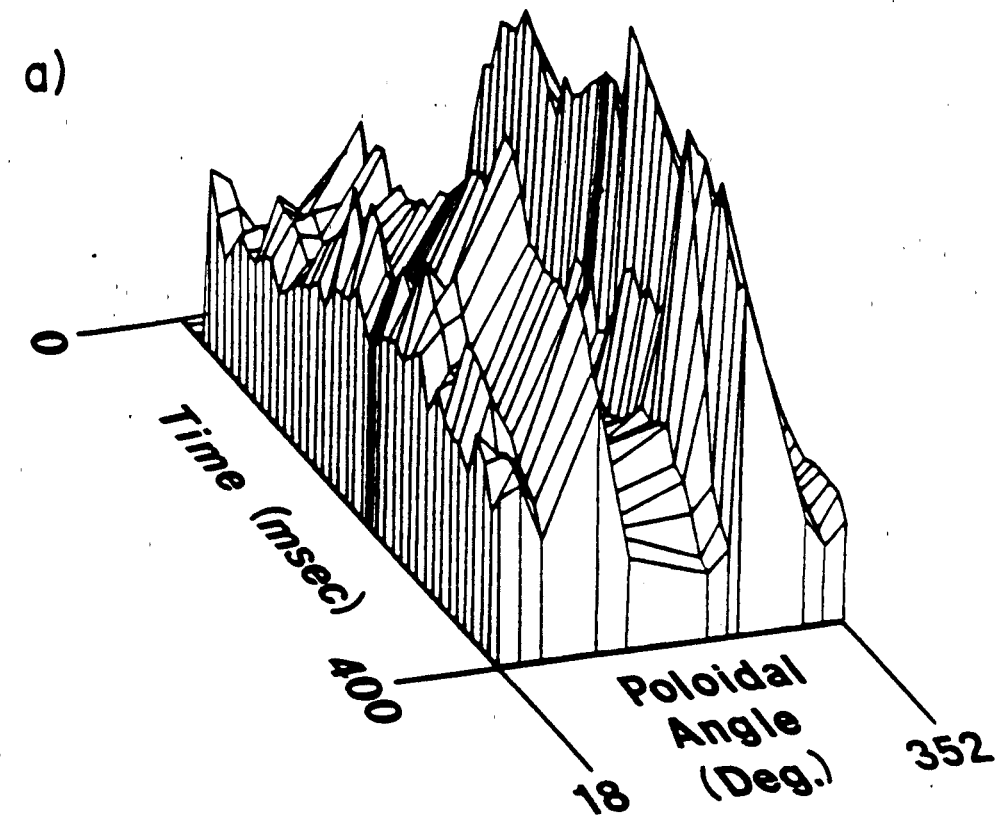
Figure 2 - Schematic diagram of the DENSEPACK probe array showing three different length Langmuir probes mounted with ~ 1 cm spacing around the poloidal circumference. The indicated poloidal coordinate system is used to present data in subsequent figures.



8103, 3.5

Figure 2

Figure 3 - (a) 3-D surface representing density at $r = 16.8$ cm vs. poloidal angle and time with (b) a corresponding single poloidal profile at $t = 250$ msec (time of flat-top current). Density minima at the inside midplane (180°) and outside midplane (0°) locations along with density maxima near top (270°) and bottom (90°) locations are clearly evident.



b)

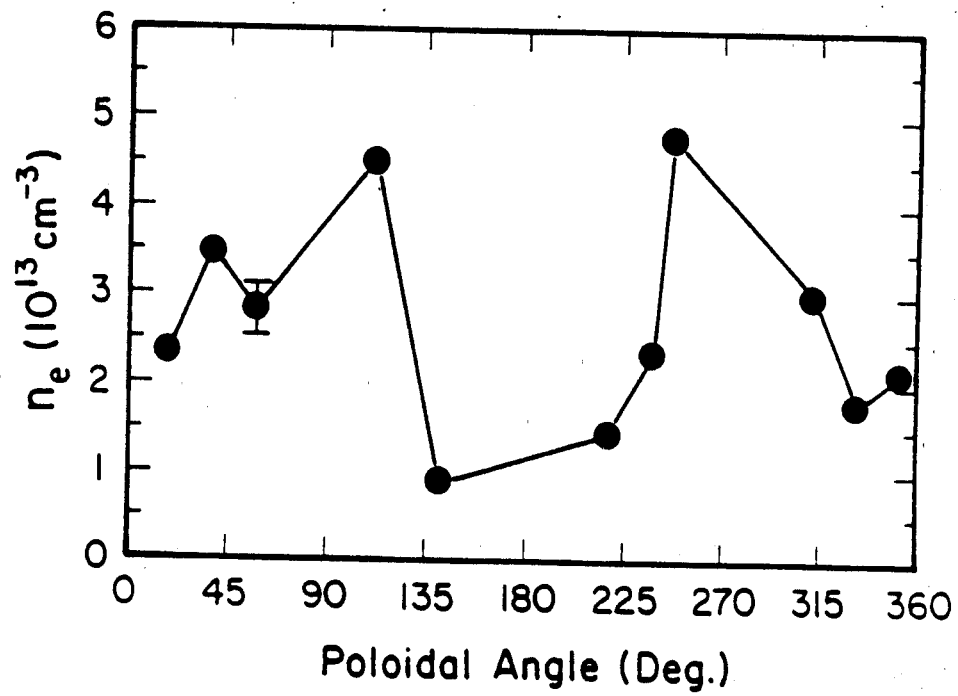


Figure 3

Figure 4 - Plasma density at $r = 16.8$ cm along the inside wall as (a) a 3-D time-angle plot and (b) a single poloidal profile at $t = 250$ msec. The high spatial resolution of this data verifies relative probe to probe calibration and shows the sharp poloidal variation across three or more probes.

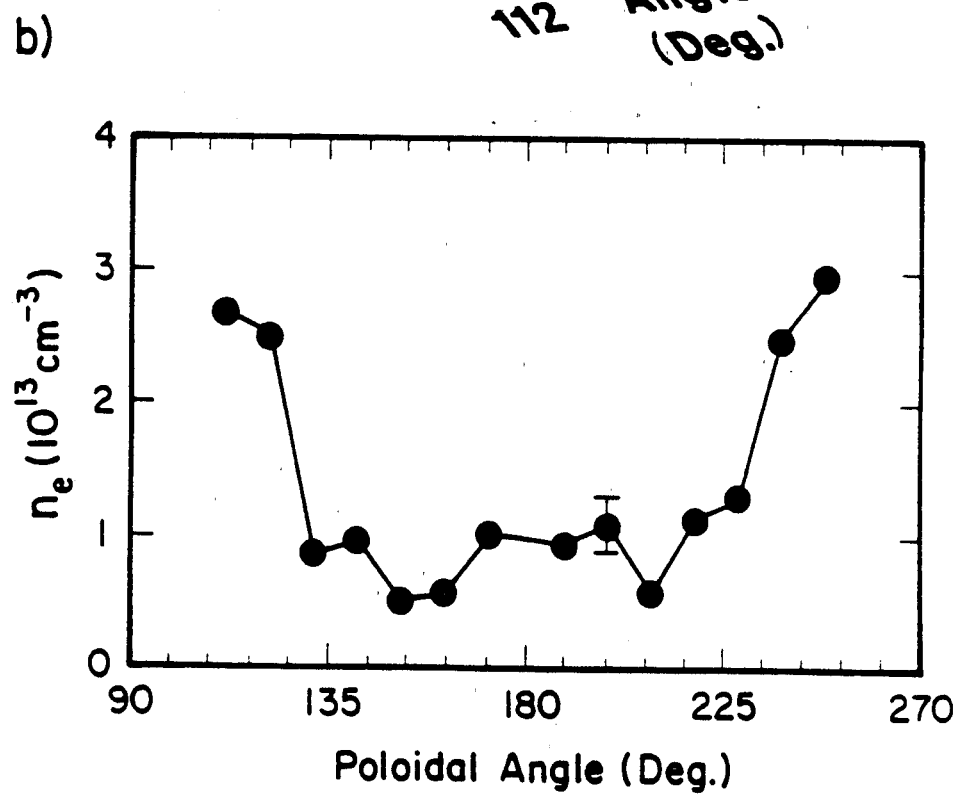
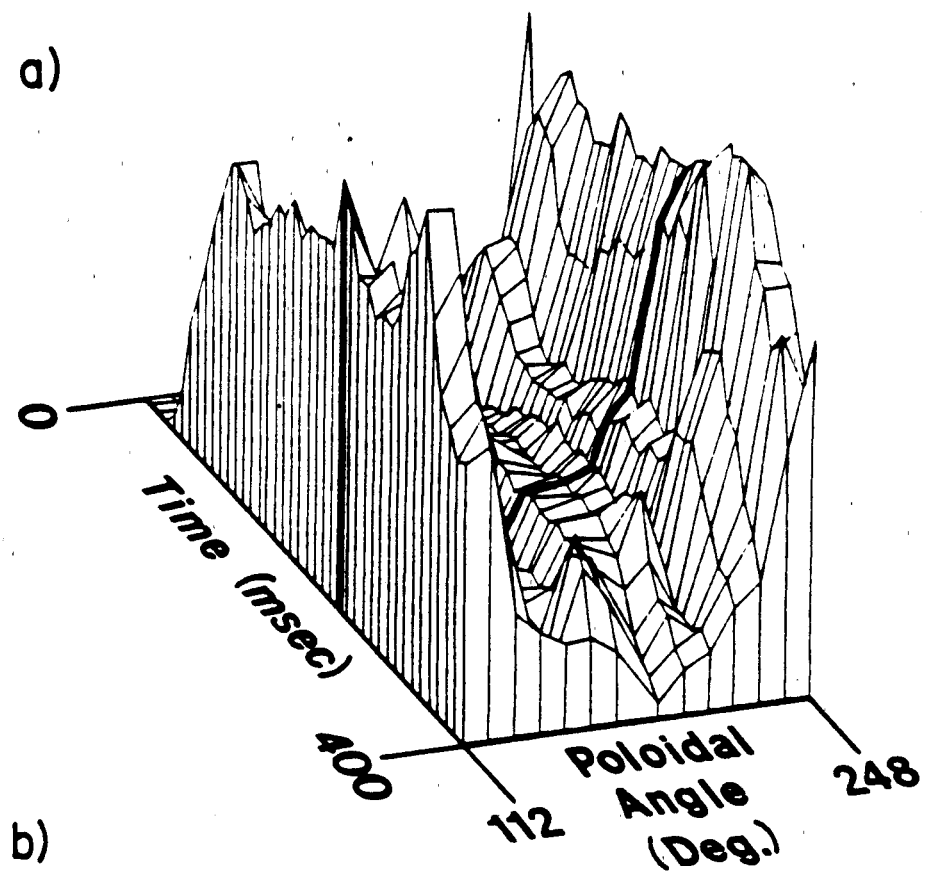


Figure 4

Figure 5 - Density in SOL plasma vs. poloidal angle and radius. Density recorded at $r = 17.2$ and 17.6 cm is scaled by $\times 2$ and $\times 4$ respectively. The poloidal structure in density is more pronounced at larger radii. Angular locations of peak density for a given radius move toward the outside midplane (360°) as r increases.

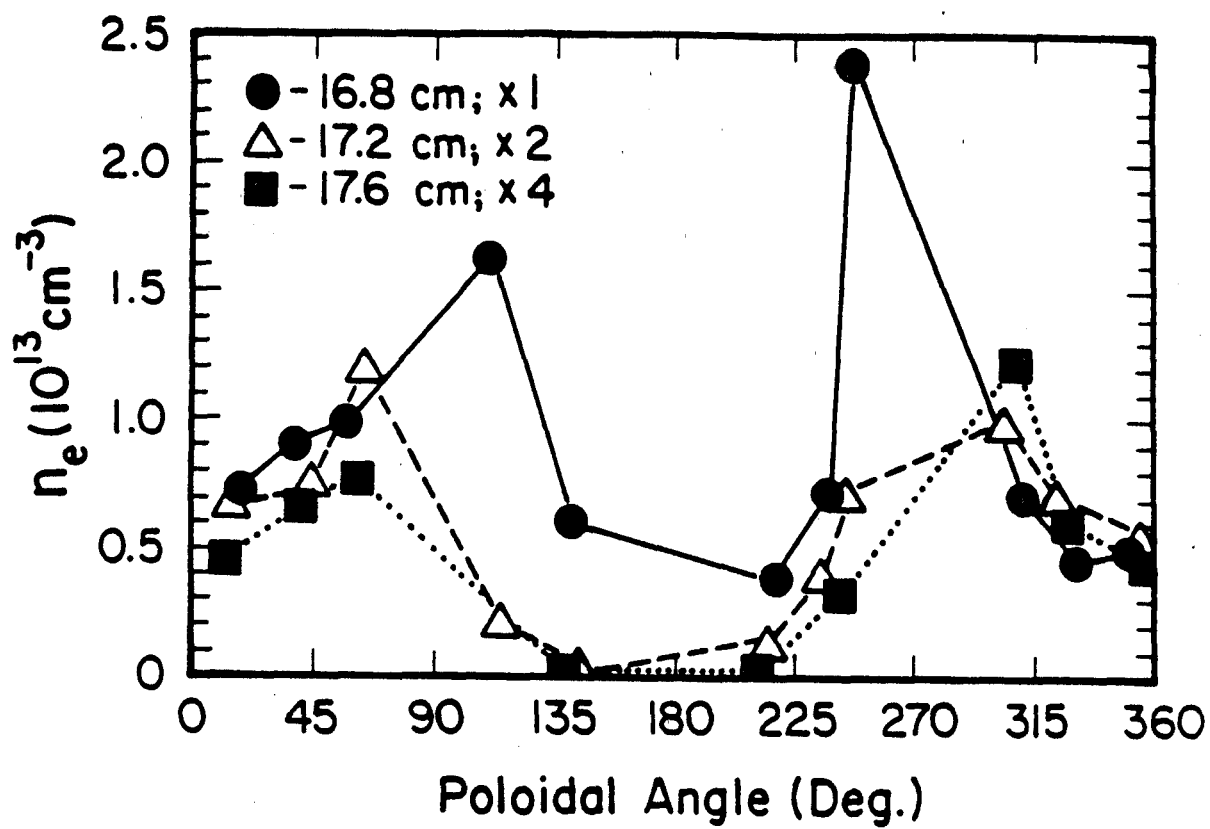


Figure 5

Figure 6 - Poloidal profile of electron temperature at $r = 16.8$ cm and $t = 250$ msec. Poloidal locations of maxima and minima in temperature roughly correspond to locations of maxima and minima in density. The lowest electron temperature at this radius is detected near $\theta \approx 225^\circ$, corresponding to the MARFE location.

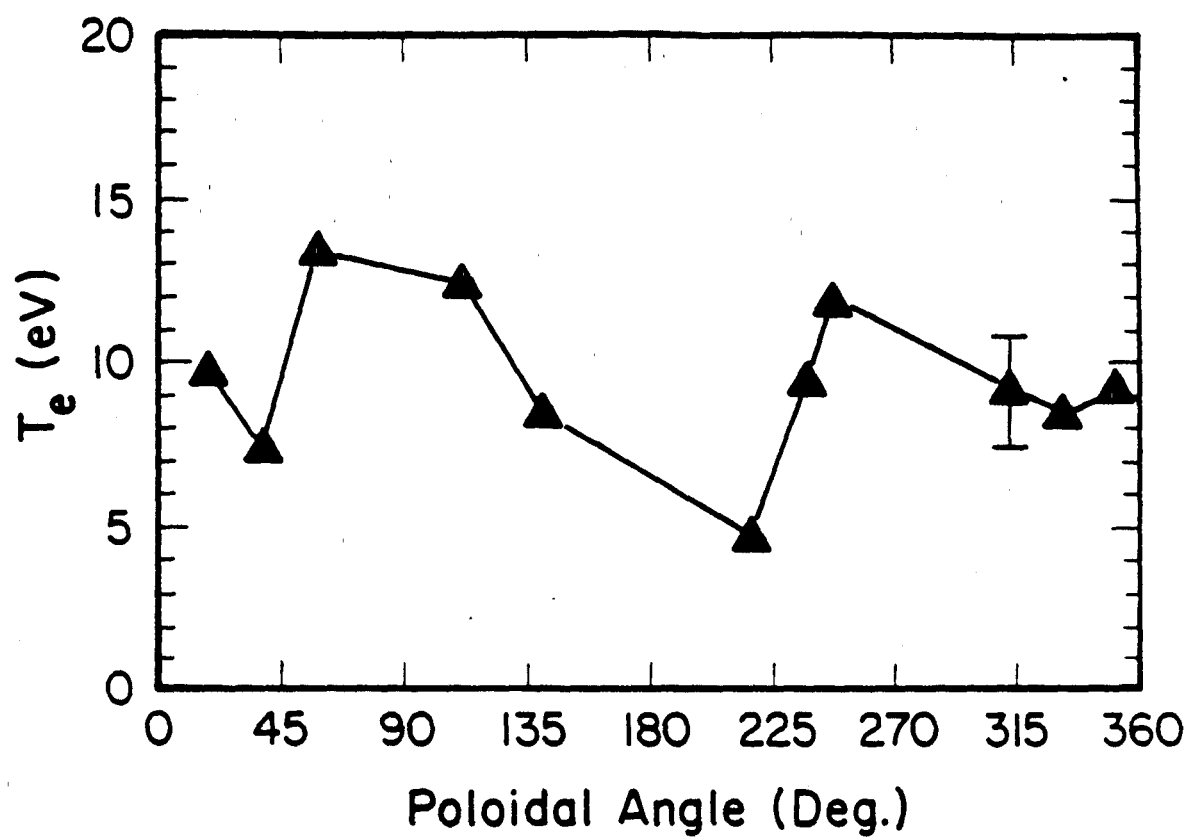


Figure 6

Figure 7 - Electron temperature in SOL plasma vs. poloidal angle and radius. Poloidal structure in temperature is not well defined at larger minor radii.

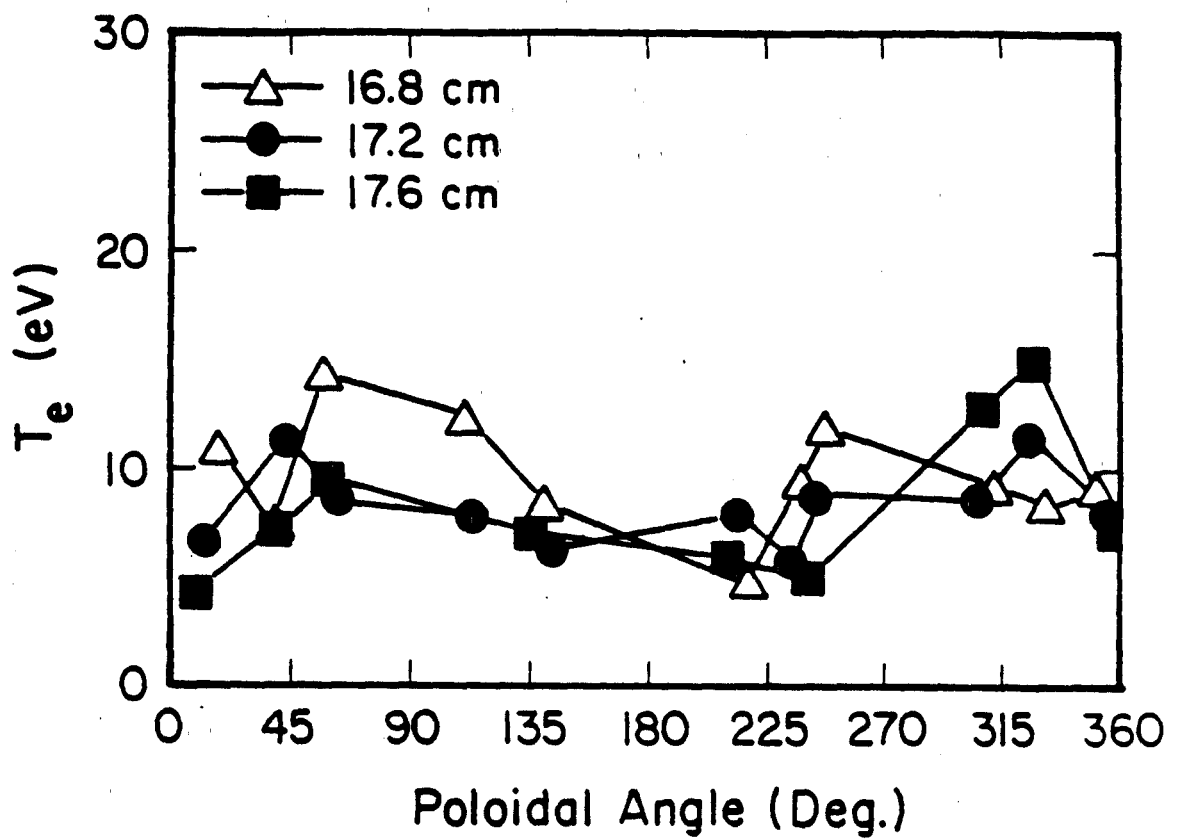


Figure 7

Figure 8 - Poloidal profile of electron pressure ($n \times T_e$) at $r = 16.8$ and $t = 250$ msec.

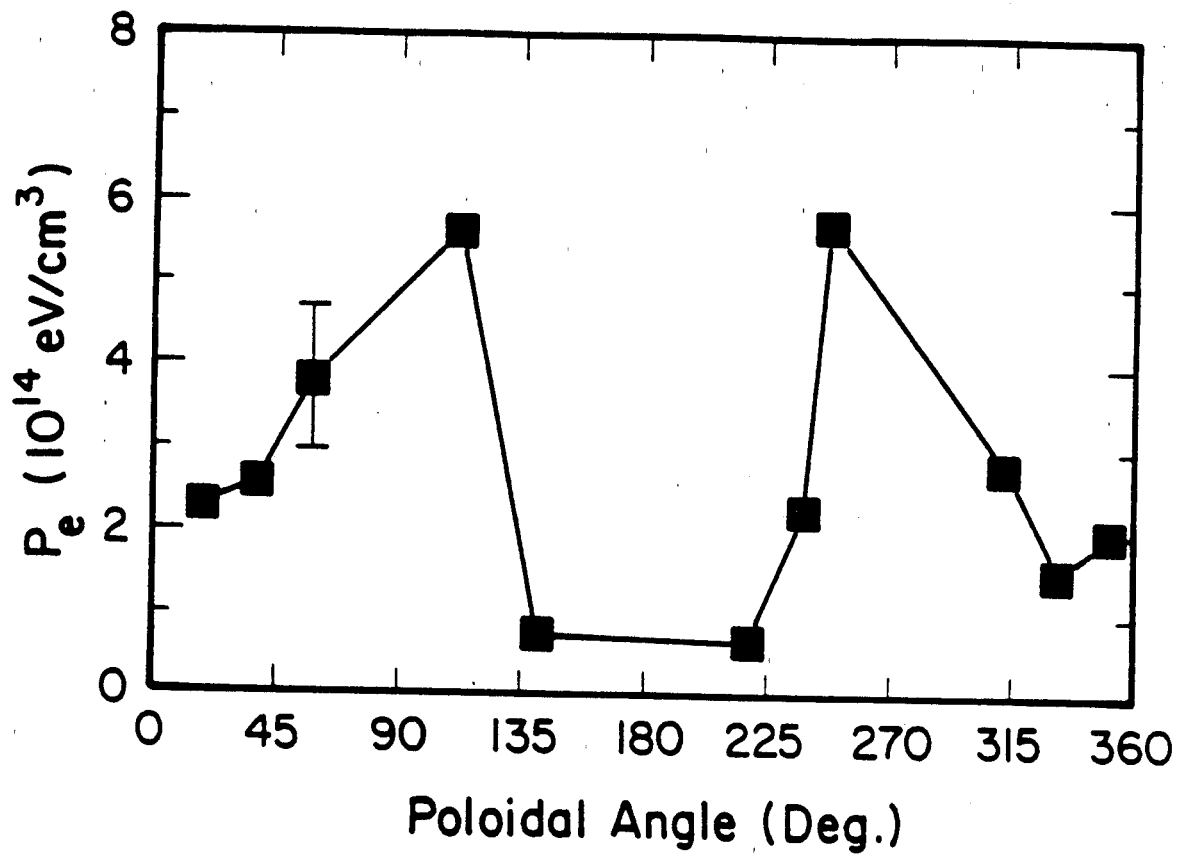


Figure 8

Figure 9 - Poloidal profile of radial density e-folding length at $t = 250$ msec.

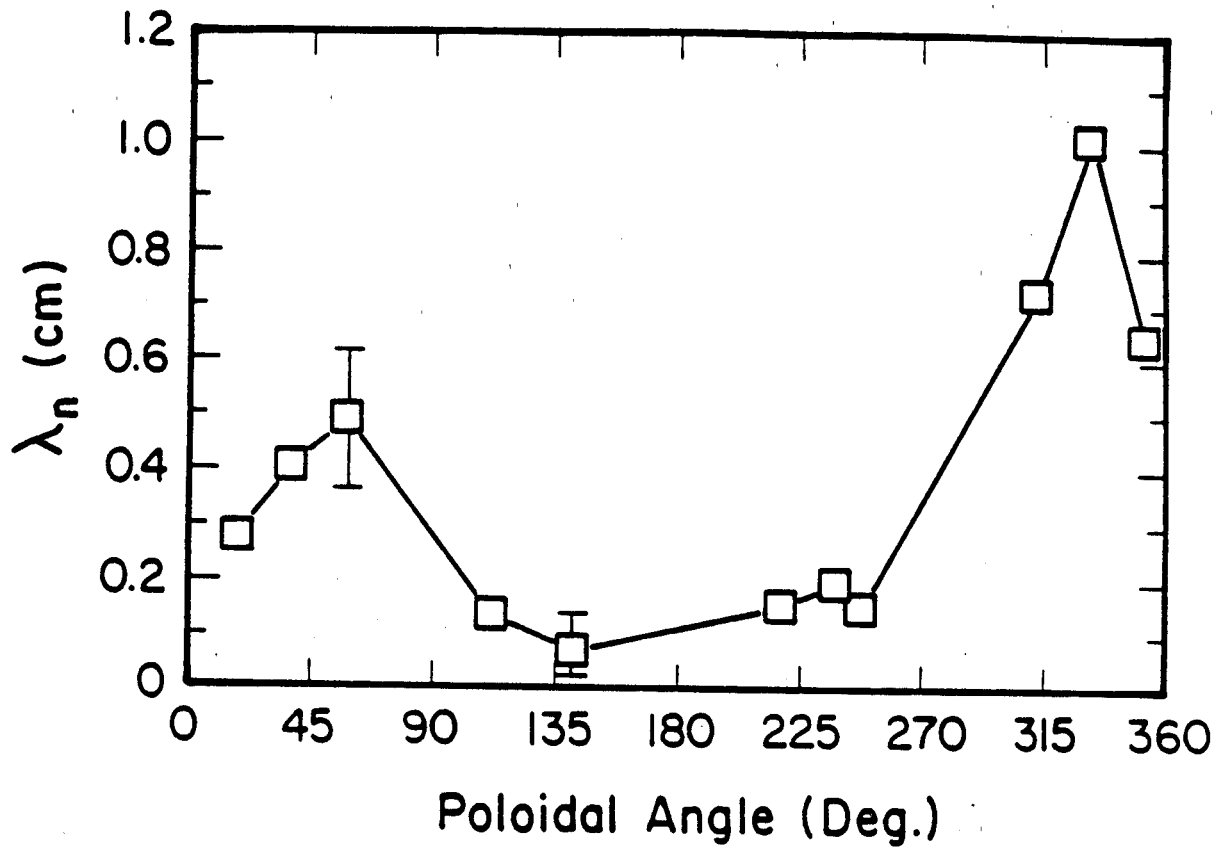


Figure 9

Figure 10 - Poloidal profile of floating potential at $r = 16.8$ cm and $t = 250$ msec.
Data collected during forward toroidal field is indicated by solid line;
reversed toroidal field by dashed line.

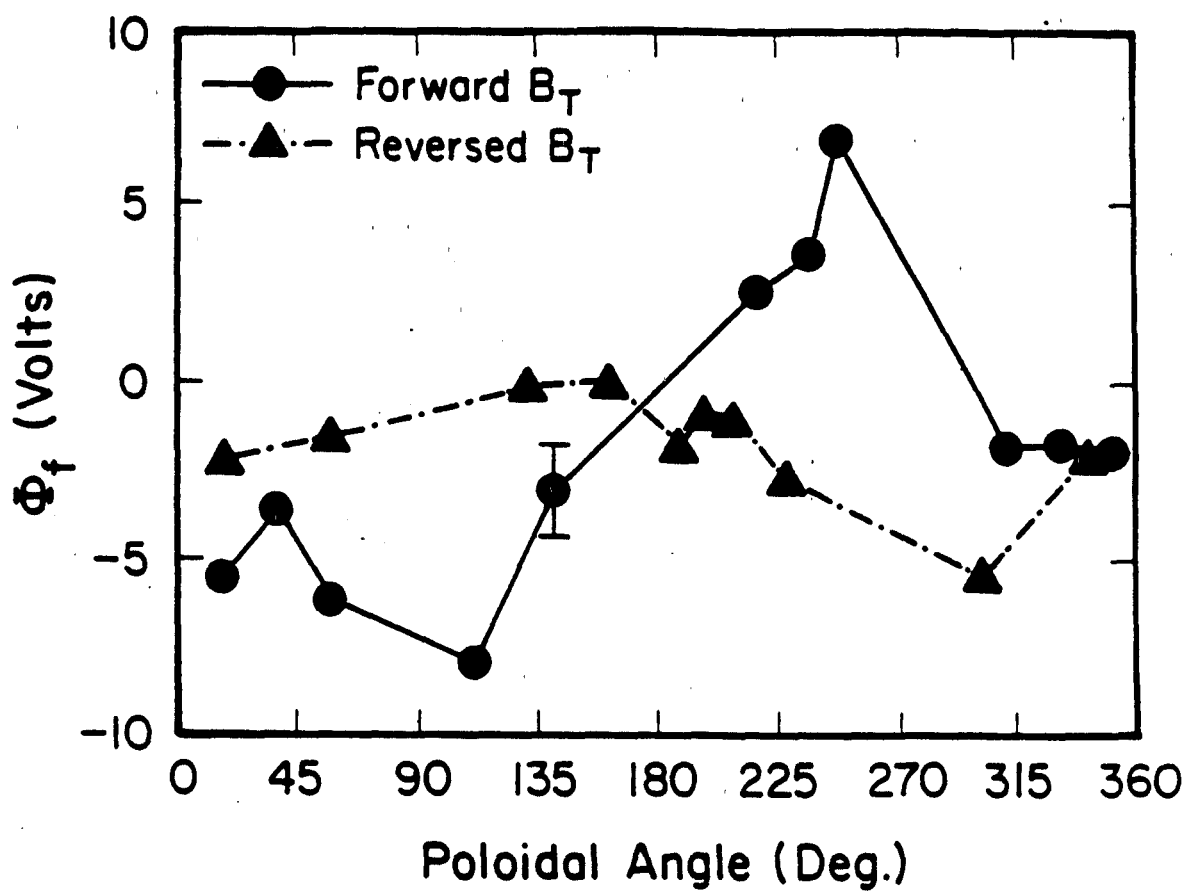


Figure 10

Figure 11 - Potential variation along a field line connecting the limiter (at 0 volt potential) with a single DENSEPACK probe. A sheath drop of $\sim 3.5 T_e$ appears before each surface. Thus, the probe floating potential approximates the plasma potential variation along a field line.

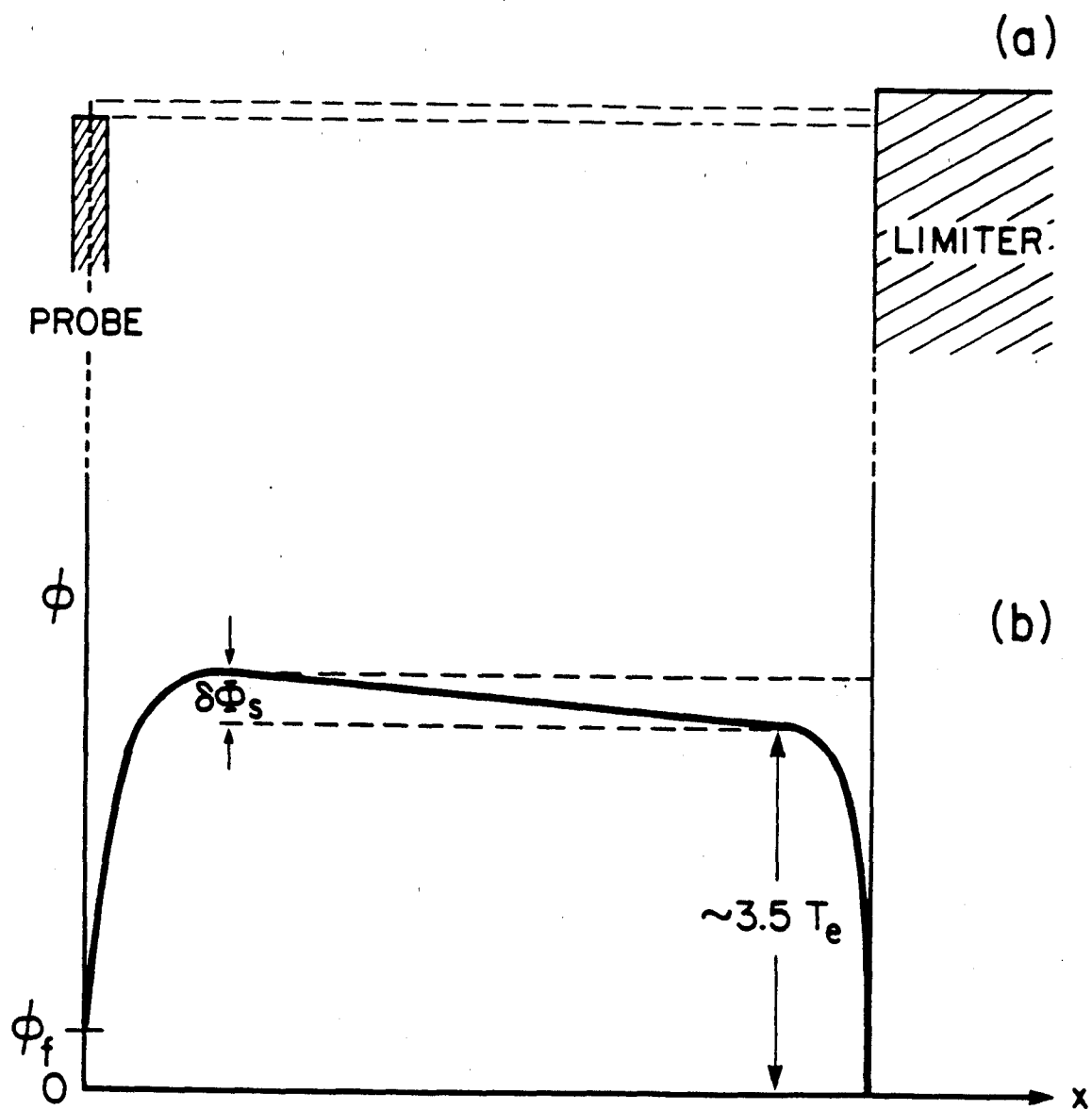
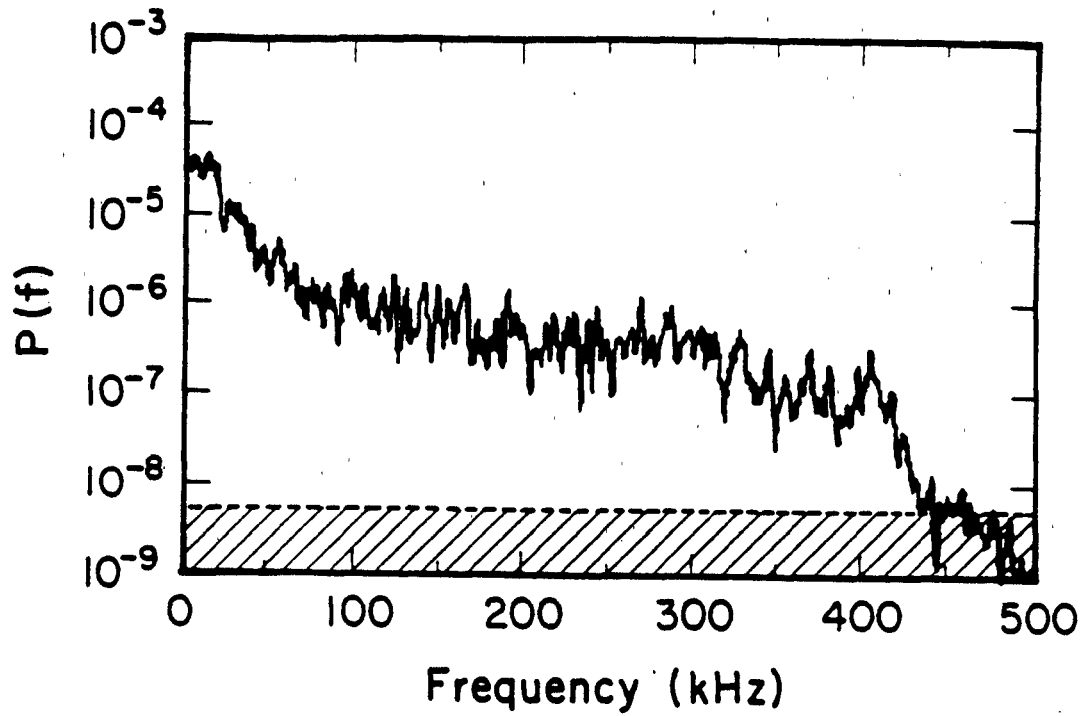


Figure 11

8103/14/11

Figure 12 - Typical \tilde{J}/\bar{J} power spectra from DENSEPACK probes as a (a) semi-log and (b) log-log plot. Spectra are found to be independent of poloidal angle. Digital noise levels are indicated as dashed lines.

(a)



(b)

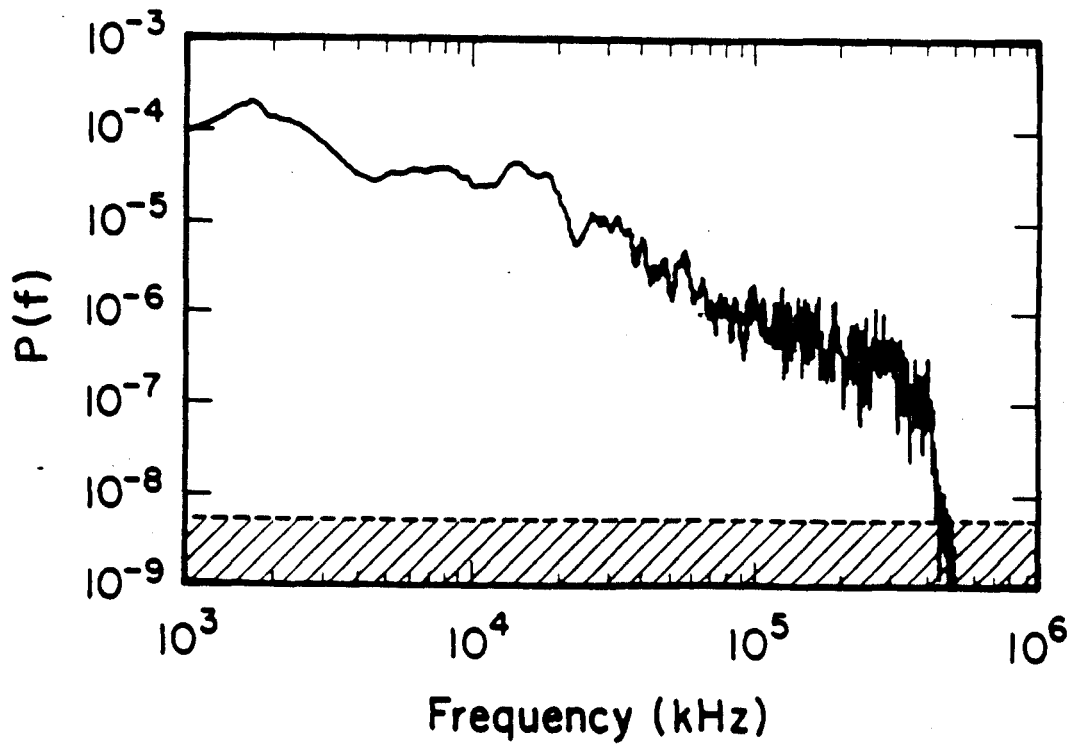


Figure 12

8103/19 14

Figure 13 - Typical autocorrelation function for a DENSEPACK Langmuir probe. The $\sin(at)/at$ structure feature disappears when more data samples are included. As shown in the expanded plot (b), typical autocorrelation times are $\tau_{corr} \approx 10\text{--}20 \mu\text{sec}$.

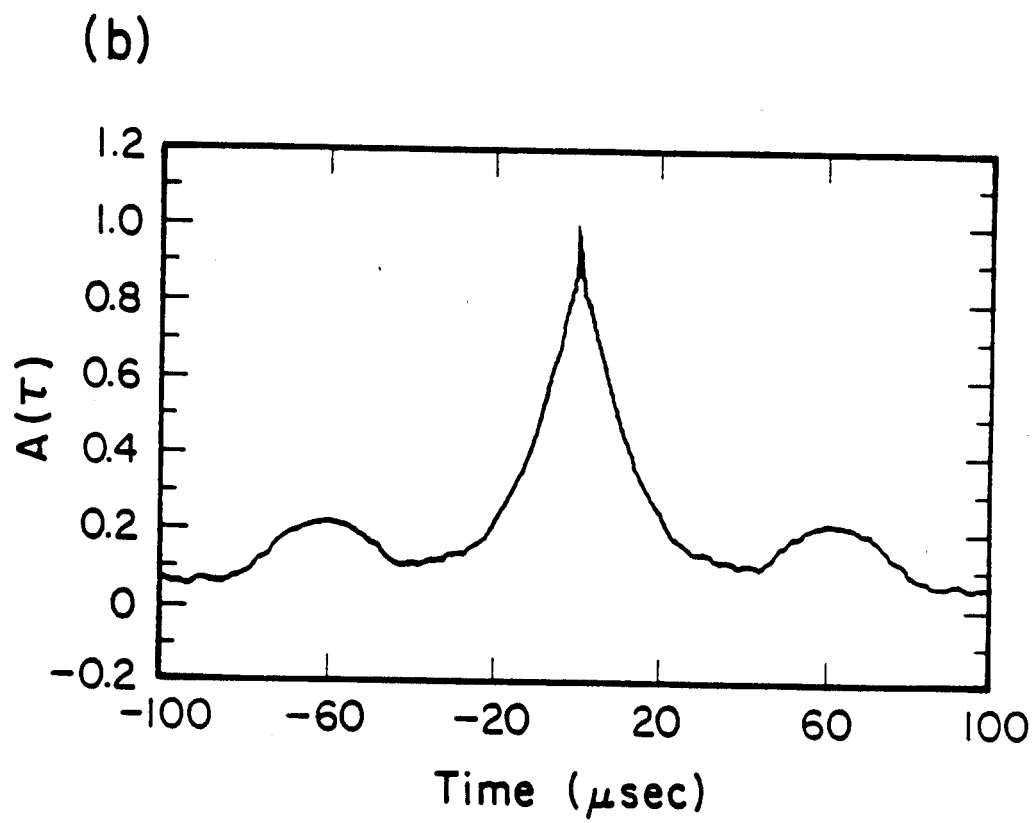
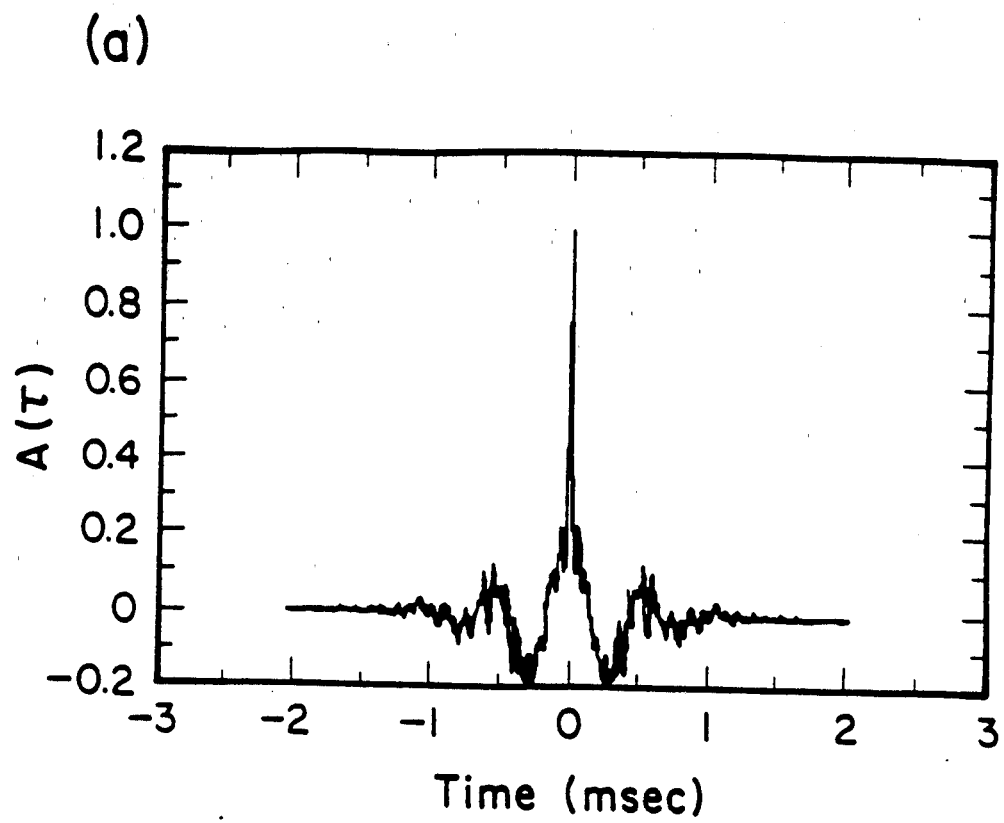
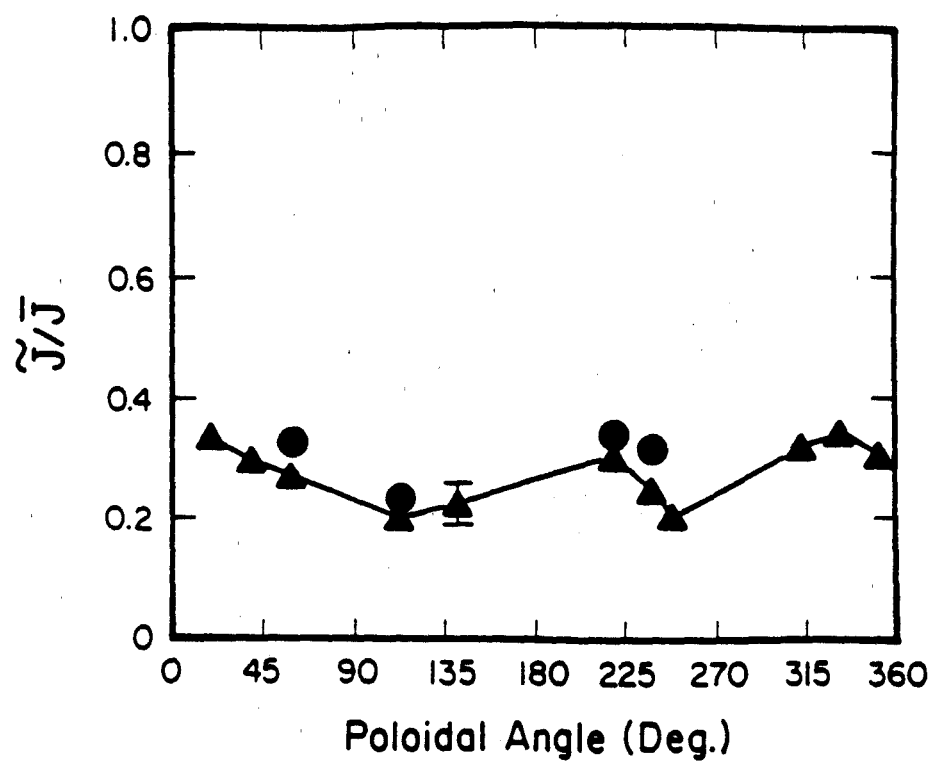


Figure 13

Figure 14 - Poloidal profile of \tilde{J}/\bar{J} at (a) $r = 16.8$ cm, and (b) $r = 17.2$ cm. 416 kHz bandwidth data is shown as solid circles; 50 kHz bandwidth as solid triangles. No correlation between poloidal variations in \tilde{J}/\bar{J} with poloidal variations in density or radial density e-folding length is found. \tilde{J}/\bar{J} computed from the 50 kHz bandwidth data is typically 80–85% of \tilde{J}/\bar{J} computed from the 416 kHz bandwidth data, independent of angle.

(a)



(b)

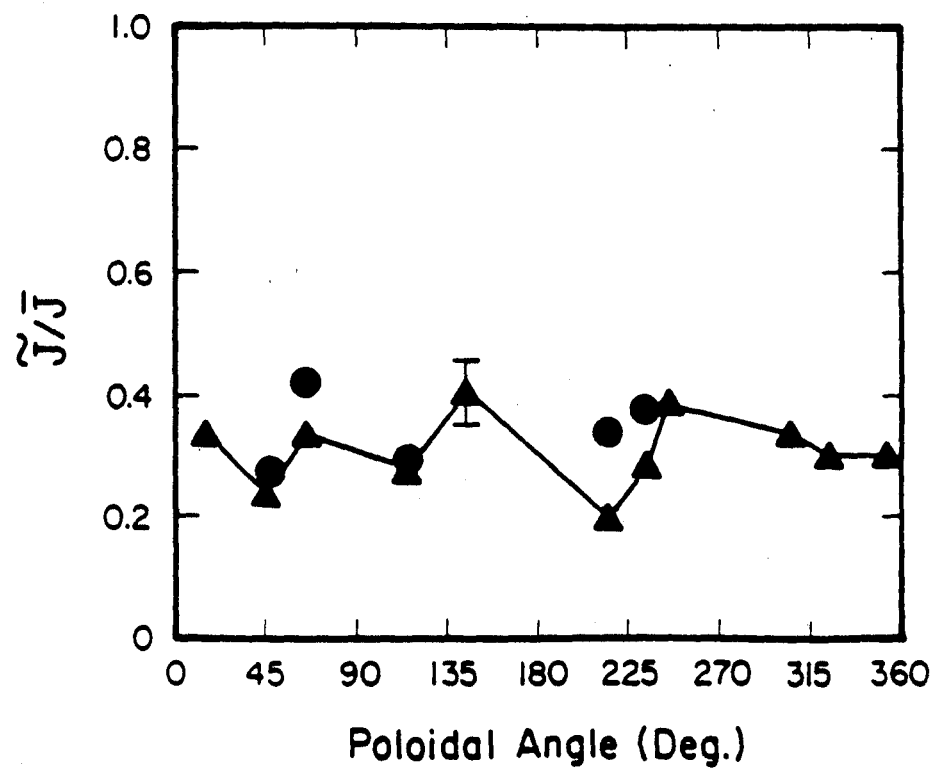


Figure 14

Figure 15 - (a) SOL plasma region sampled by DENSEPACK, and (b) conformal mapping used to display data in subsequent plots.

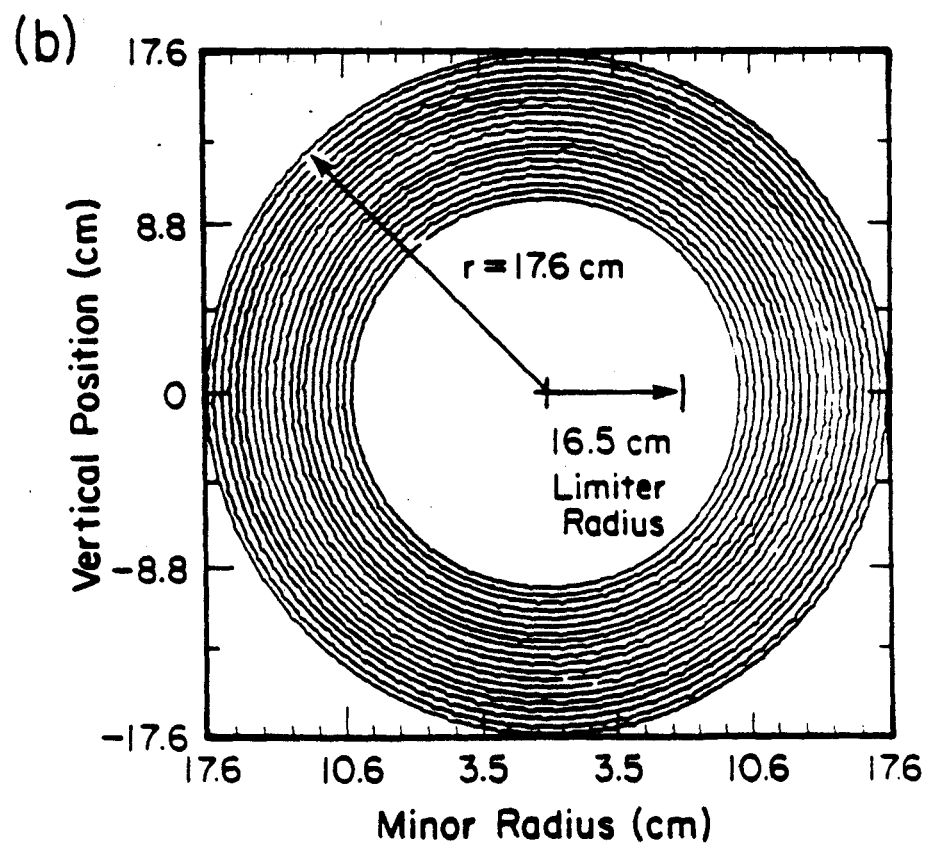
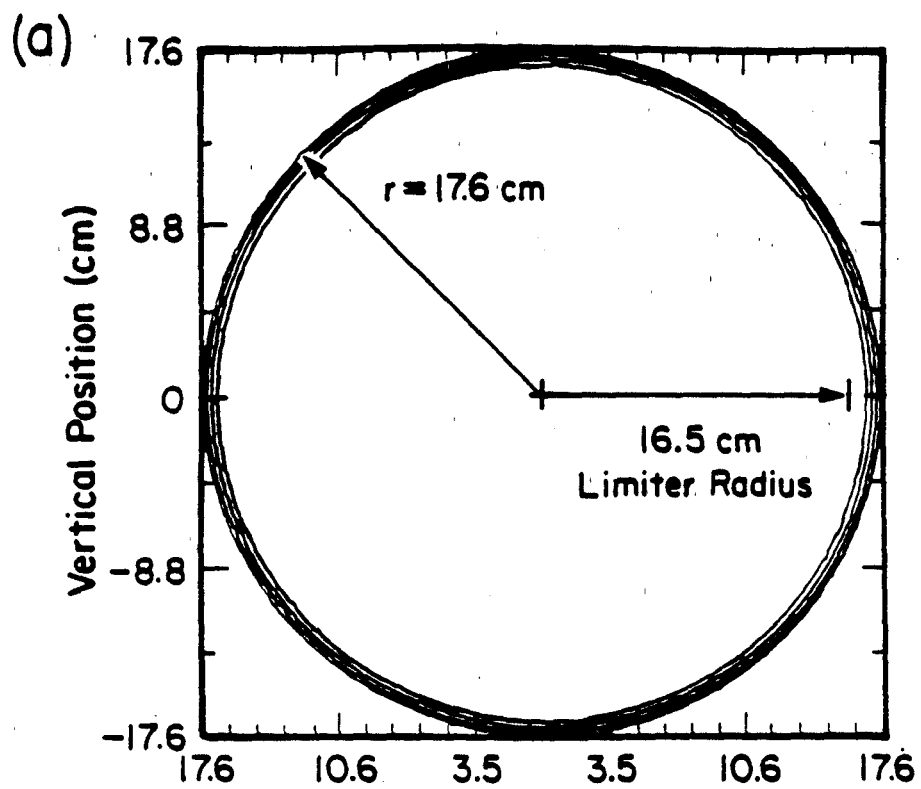
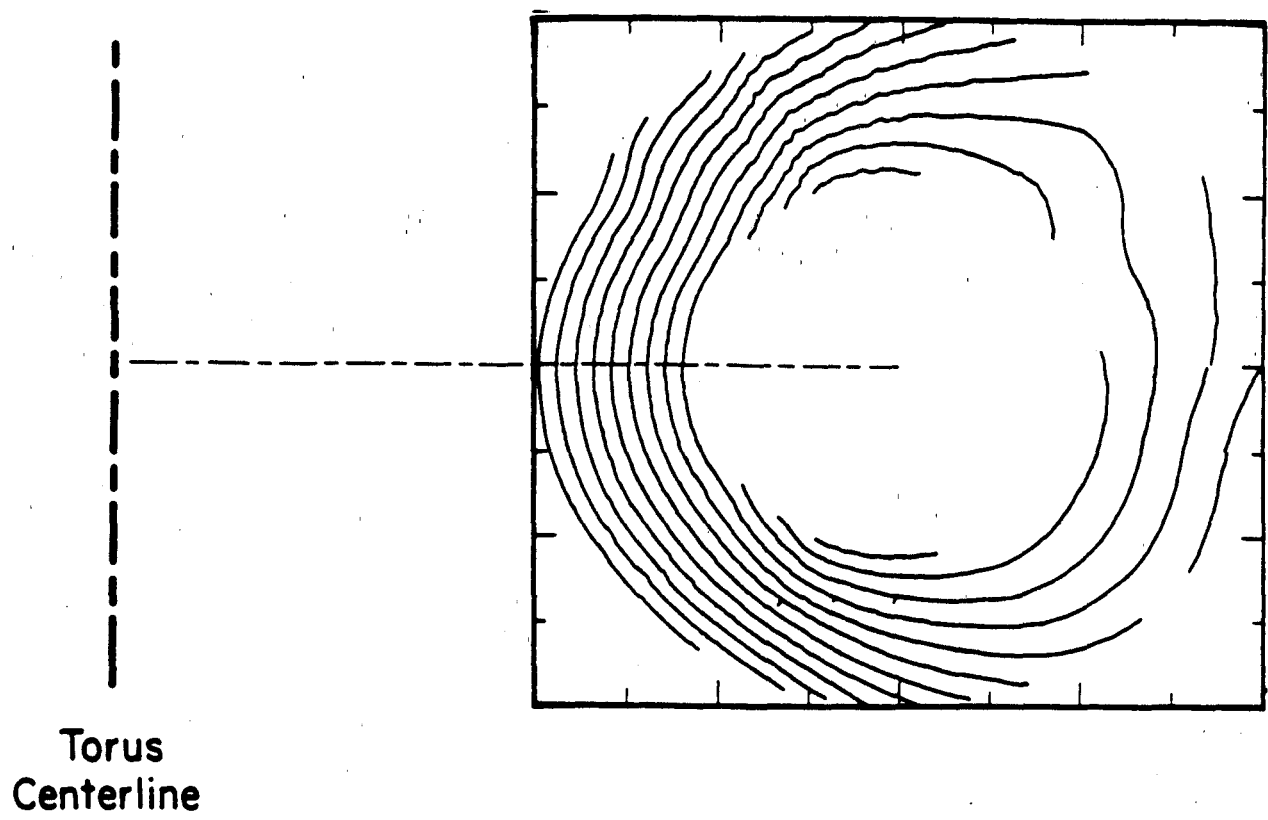


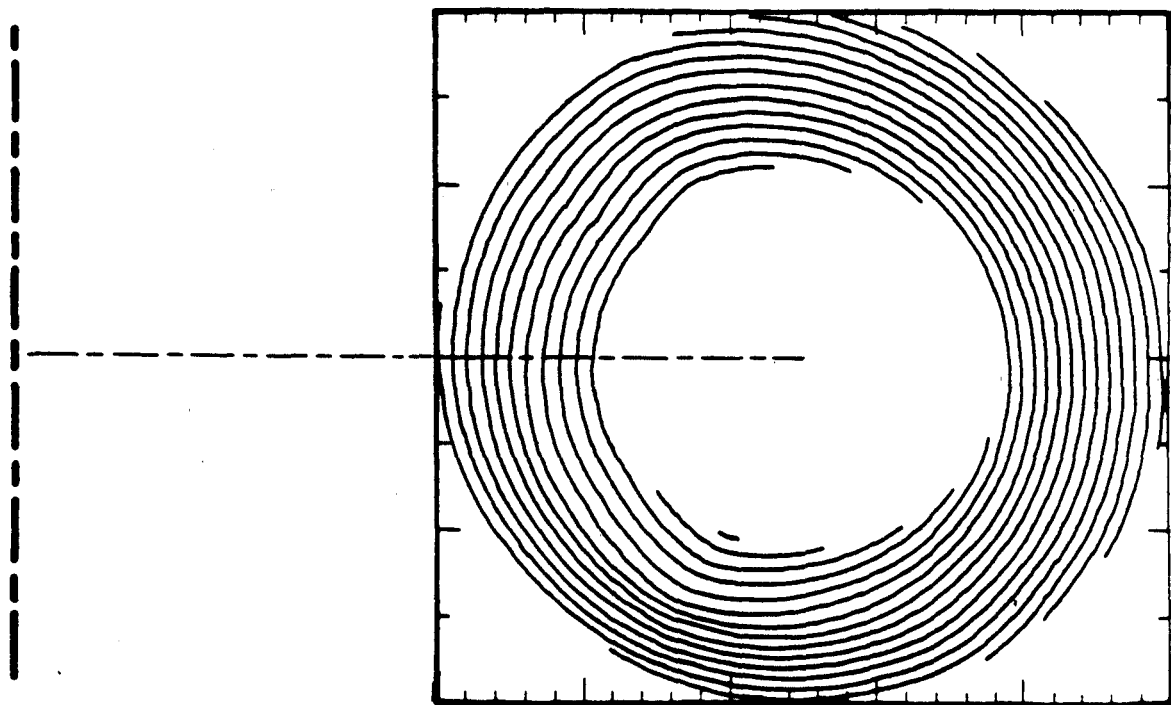
Figure 15

Figure 16 - (a) Constant electron pressure surfaces inferred by DENSEPACK at $t = 250$ msec ($P_e = n \times T_e$), and (b) flux surfaces inferred simultaneously by an array of 12 magnetic loops. The conformal mapping clearly shows that $P_e \not\approx \text{const.}$ on a flux surface.

(a)



(b)

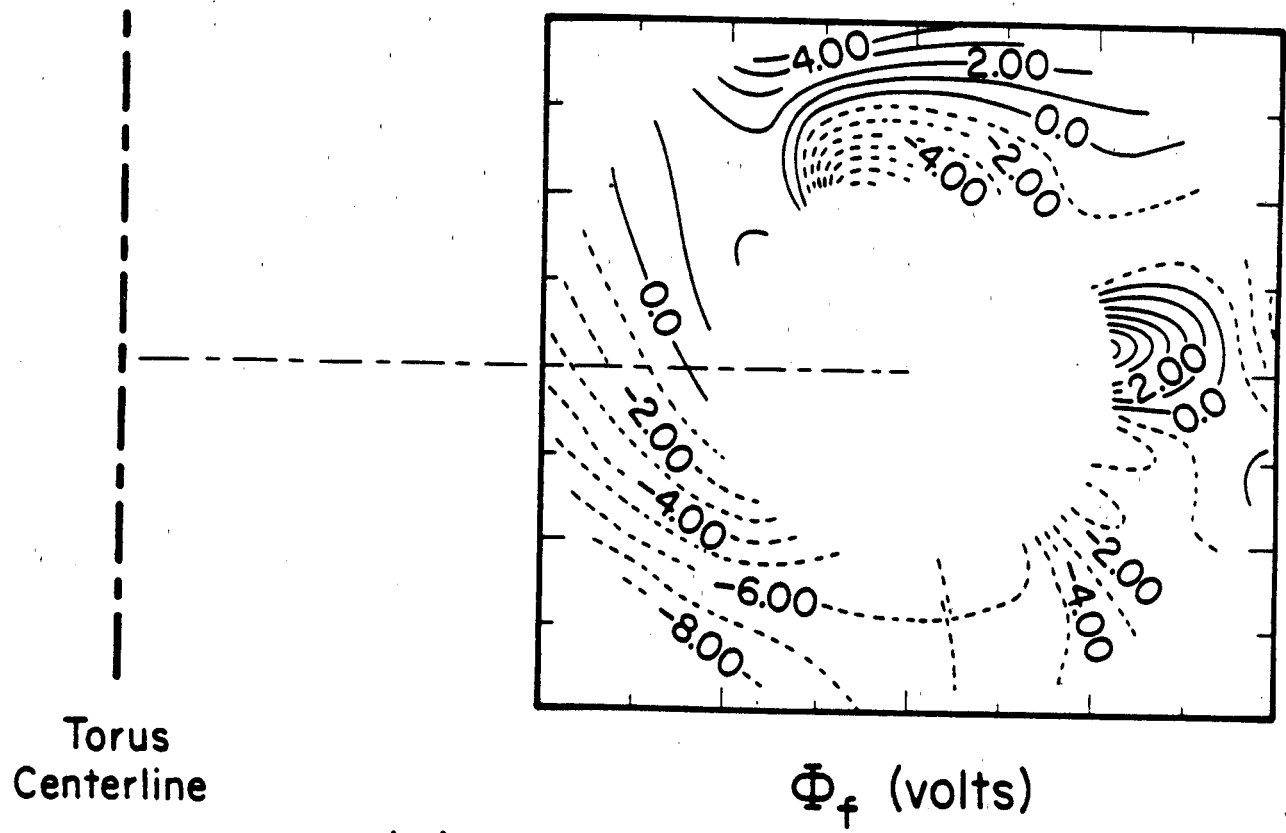


8103, 7/8

Figure 16

Figure 17 - (a) Contours of constant floating potential (Φ_f), and (b) contours of constant space potential (Φ_s) on conformally mapped SOL region. Labels correspond to contour potentials in volts.

(a)



(b)

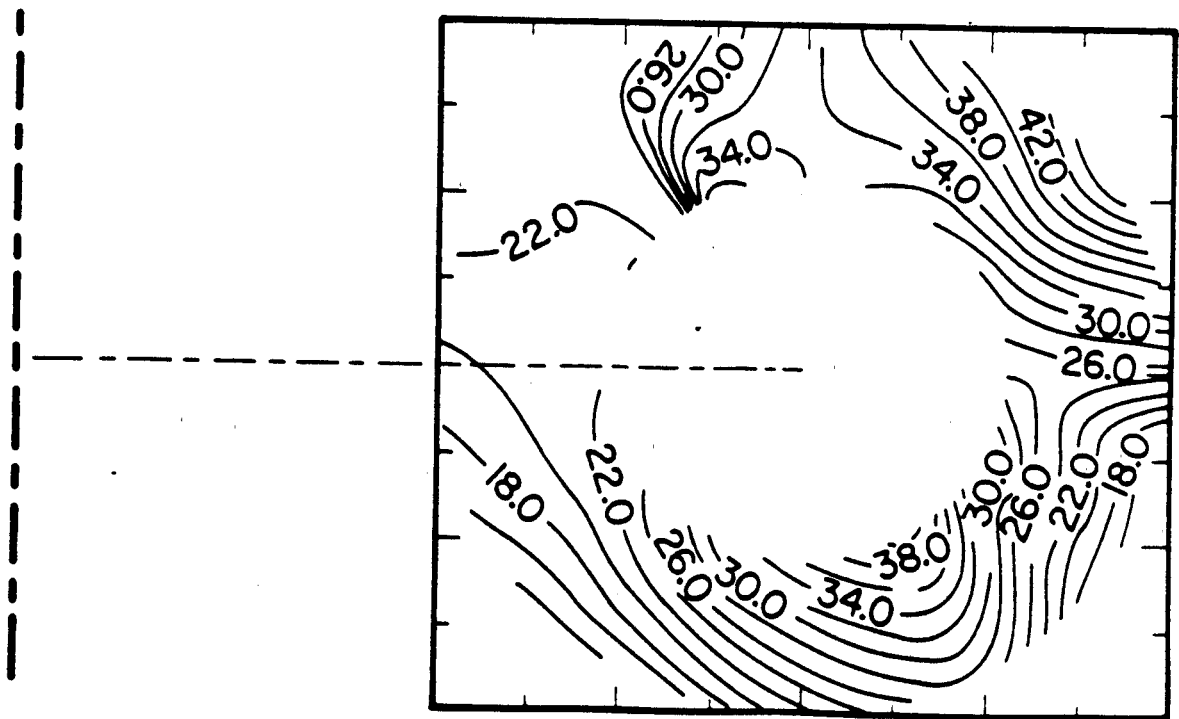
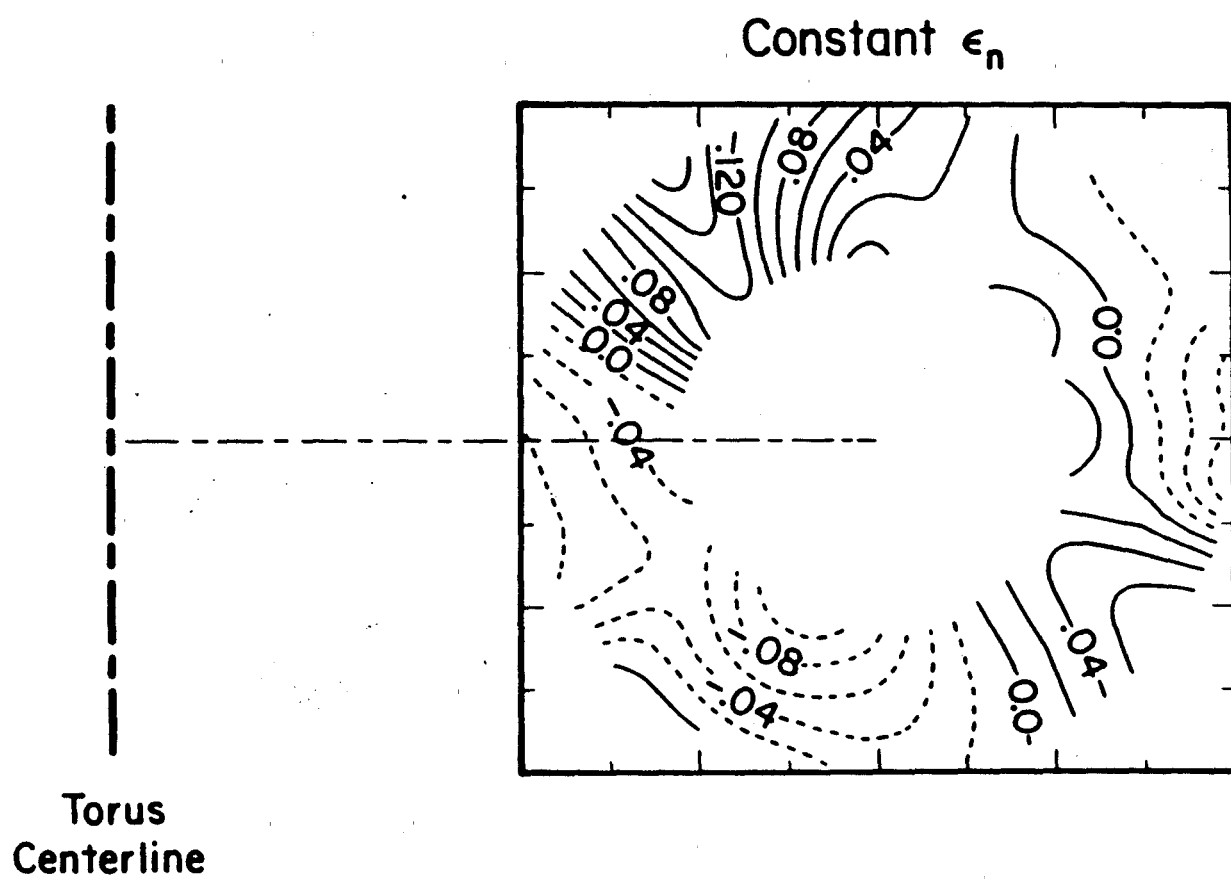


Figure 17 Φ_s (volts)

8103.9

Figure 18 - Contours of constant ϵ_n on conformally mapped SOL region. $|\epsilon_n|$ indicates the relative importance of steady state $\underline{E} \times \underline{B}$ convection on the equilibrium density profile. Pattern indicates that $\underline{E} \times \underline{B}$ fluxes are not sufficient to explain poloidal asymmetry in density.



8/03/19/9

Figure 18

Figure 19 - Poloidal profiles of (a) radial density e-folding length and (b) density extrapolated to the limiter radii at $t = 250$ msec. Poloidal asymmetry in density is found to persist at limiter radius and indicates that plasma outside the SOL region ($r \lesssim a$) also exhibits strong poloidal asymmetries. Path of inside density interferometer laser beam is shown as dashed lines.

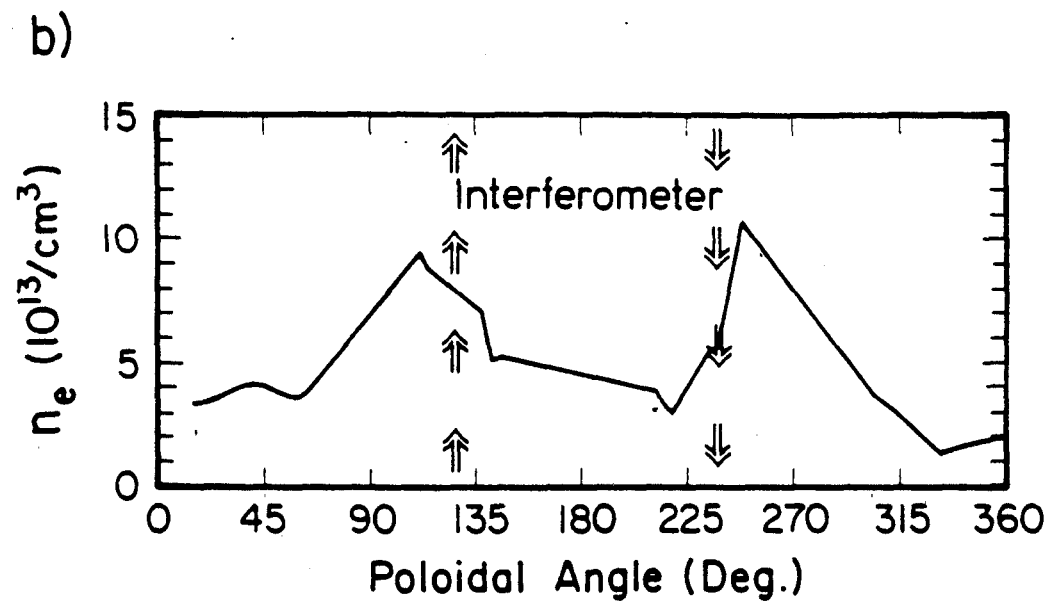
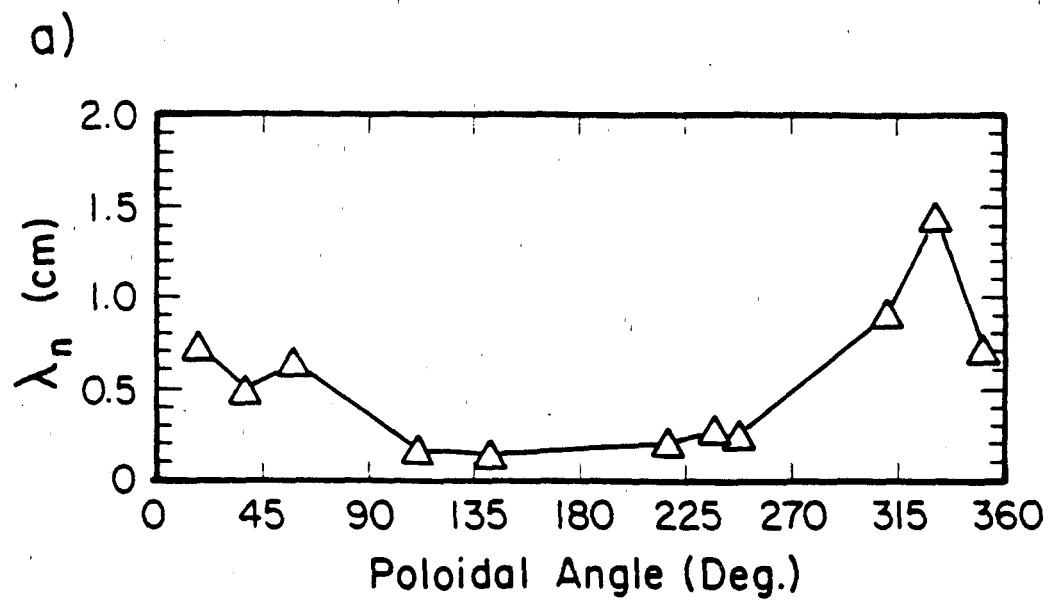


Figure 19

8103/19, 5

